Numerical investigation of the effect of a transducer pulse on the microfluidic control of a piezoelectric printhead

Jr-Ming Lai
Jenn-Der Lin
National Chiao Tung University
Department of Mechanical Engineering
1001 Ta Hsueh Road
Hsinchu 30050, Taiwan
E-mail: jdlin@cc.nctu.edu.tw

Kung Linliu
National Synchrotron Radiation Research Center
Scientific Research/Facility Utilization
101 Hsin-Ann Road
Hsinchu Science Park
Hsinchu 30076, Taiwan

Abstract. Numerical calculations are performed to investigate the effect of the component of a single transducer pulse on the ejection of a drop for a drop-on-demand ink-jet printhead with a piezoelectric actuator. The flow field is governed by continuity and Navier-Stokes equations. A volume-of-fluid method with a piecewise-linear interface construction is used to track the complicated topological variation of the liquid-gas interface. The computer code is validated with experimental results present in the literature. The volume of the primary drop is closely related to the maximum displacement D_f of chamber wall induced by the piezoelectric actuator in the forward stoke; the velocity of the primary drop depends on the ratio of D_f to the time period of the forward stoke $\Delta\tau_f$. Moreover, the fact that the formation of the primary drop depends weakly on the conditions of the backward stroke is considered. A decreased interval between forward and backward strokes might serve to suppress the formation of satellite drops owing to reducing the liquid thread length l_b at pinching off to a value less than the upper limit l_b'. The breaking up of the freely flying liquid thread from nozzle outlet has two modes—multiple breaking up and end pinching—and depends on the thread length at pinching off. © *2010 Society of Photo-Optical Instrumentation Engineers.*
[DOI: 10.1117/1.3486201]

1 Introduction

In a search for new methods to fabricate oligonucleotide microarrays,[1] color filters for liquid-crystal display panels,[2] multicolor polymer light-emitting-diode displays[3] and transistors,[4] and to visualize protein distributions[5] attention to ink-jet printing has increased. Ink-jet printheads comprise two main types—continuous ink jets (CIJ) and drop-on-demand (DOD) ink jets. In the CIJ printhead, liquid emerges continuously from a nozzle to form a jet on compressing the chamber ink sufficiently, therefore disintegrating into a train of drops through Rayleigh instability.[6,7] In contrast, liquid remains in a DOD printhead nozzle, forming a meniscus unless pressure is applied to overcome the surface tension.[8] Because of its simplicity and the feasibility of a decreased size of the system, the DOD printhead has a major share of the market of ink-jet printers.

The basic configuration of an ink-jet device is, in general, composed of a chamber with one open end, called a nozzle, from which a liquid jet emanates to disintegrate into drops; the other end is connected to a fluid reservoir that supplies the liquid necessary to produce the next drop. Most commercial DOD ink-jet printers use either a thermal or a piezoelectric method as actuation to transform an electric signal into the motion of a fluid.[8] In the thermal ink-jet device, the expansion of a vapor bubble, induced by an electrically commanded miniature heater, forces the fluid into motion. Piezoelectric ink-jet devices substitute the deformation of an electrically commanded solid sheet instead of a bubble expansion.[8,9] To actuate the piezoelectric material or the heating element, an excitation signal, typically a pulse, must be incorporated. The great advantage of the thermal ink-jet device is that it can be produced with a microelectromechanical system (MEMS), but its brief lifetime constitutes a great disadvantage.[8,10] In addition, liquid in the thermal device must be heated and vaporized to form a bubble as a pump. This heating might cause chemical alteration of the properties of the liquid, thereby limiting the applications of this device. The piezoelectric ink-jet device is extensively exploited for its reliability and adaptability in various applications of microfluidic control, even though the means of production and a high driven-voltage pulse entail great cost. To improve a DOD ink-jet printhead and its applications to the fabrications already mentioned, the ejection of drops should be comprehended fully. This ejection behavior involves complicated fluid mechanics including a competition among viscous, capillary, inertial, and contact-line forces. Varied research is reported in the literature.

An experiment to investigate the fluid mechanics of a drop ejection depends mainly on stroboscopic observation. The basic principle of this method is that the region of interest, in which liquid emerges in the form of a jet that subsequently disintegrates into drops, is illuminated with a

pulsed light such as a light-emitting diode (LED). The images of the ejected liquid are recorded with a camera incorporating a charge-coupled device (CCD) associated with a microscope. The stroboscope light is generally synchronized with the CCD camera. Many experimenters have visualized the liquid jet and the formation of a drop from DOD ink-jet printheads.[11–16] For instance, Meinhart and Zhang[14] utilized a particle-image-velocimetry system with micrometer resolution to measure simultaneously the velocity flow field with spatial resolution to 5 to 10 μm and temporal resolution to 2 to 5 μs. Fan et al.[12] assessed the drop quality from a temporal sequence of magnified images recorded with a CCD camera and a stroboscopic technique while varying the nozzle size, voltage signal, and liquid properties. Kwon[13] developed edge-detection techniques for the jet speed and drop diameter using CCD camera images with a varied trigger interval. Moreover, Dong et al.[16] used stroboscopic photography to capture sequential images of the drop ejection process from a piezoelectric ink-jet printhead. In this study, several key stages of DOD drop formation were identified and quantitative analysis of the dynamics of drop formation was developed.

The prediction of droplet formation, which can not only validate theoretical models with experimental observation but also provide insight into asymptotic conditions, constitutes a substantial challenge to numerical simulation. Early models failed to predict the temporal evolution of the velocity, shape, and trajectory of a drop because models of interfacial physics were inadequate and topology variations were complicated.[17–21] As numerical methods have developed and computing power has advanced, computational fluid dynamics (CFD) has become a promising tool to overcome the limitations of theoretical models. Among diverse approaches, the volume-of-fluid (VOF) method proposed by Hirt and Nichols[22] proved to be effective for its simplicity and robustness.[23–29] Wu et al.[28] demonstrated the feasibility of the full cycle of ink-jet printing including the ejection, formation, and collision of drops against a target substrate with their custom program; employing a finite-difference-based method to solve fluid dynamics and the VOF method to capture the variation of the interface, this program was validated with experimental observation. Liou et al.[25] simulated the ejection of a printhead (SEAJet) by applying commercial CFD software (COMET, StarCD Suite) based on the VOF method to handle free-surface problems. The software discretizes governing equations by means of a finite-volume approach and exploits the continuum-surface-force (CSF) model to account for the effect of surface tension; the predicted evolution of the meniscus inside the printhead was compared with published experimental results. Pan et al.[27] used commercial CFD software (Flow-3D) to simulate the drop formation of a drop ejector with a microelectromechanical diaphragm and provided useful information concerning the design of this ejector; the software was tested to be capable of modeling the free-surface problems, employing the finite-volume approach to solve the governing equations of fluid flow and the VOF method to track effectively the interface deformations. Feng[23] conducted various numerical experiments to find design rules of ink-jet devices utilizing the same software (Flow-3D); the volume, velocity, and shape of drops were chosen to evaluate the jet performance. Yang et al.[29]

exploited commercial software (CFD-ACE+), also applying the VOF approach for interface tracking to explore numerically the drop ejection of a printhead (Picojet); 17 simulation cases were undertaken to reveal the design concept of the printhead. Although other numerical methods have been proposed,[30,31] the VOF methods are considered to be commonly used for the modeling of the drop formation in DOD ink-jet printheads.

The full theoretical model of the piezoelectric DOD ink-jet printhead involves the coupling of structural, electric, and interfacial flow fields. The direct coupled-field simulation of this printhead might require substantial computing power and cost. An alternative method, so-called load transfer, coupling multiple fields on applying results from one analysis as load in another analysis, might be effective to simulate the multiphysics of a piezoelectric DOD ink-jet printhead. Several authors[19,28,29,31,32] have shown the feasibility of the load-transfer method to simulate the full system of the piezoelectric printhead. Wu et al.[28] used the propagation theory of acoustic waves before the simulation of interfacial flow of piezoelectric ink-jet printing to estimate the temporal variation of pressure imposed at a location upstream from the nozzle outlet as a boundary condition on pressure. Yu et al.[31] coupled an interfacial flow solver with an equivalent circuit model that transfers the effect of the ink cartridge, supply channel, vibration plate, and piezoelectric actuator into the pressure at the nozzle inflow with a given voltage signal. Kim et al.[32] measured the displacement waveform from a piezoelectric actuator with a laser Doppler vibrometer (LDV); this waveform information then served as input data at the piston-moving boundary for the 3-D simulation of an ink jet. Chen et al.[19] used finite-element software (ANSYS) to determine the temporally dependent averaged moving velocity of the piezoelectric diaphragm; this velocity was imposed as an inflow boundary condition in a drop ejection simulation of an ink-jet printhead. Yang et al.[29] reported that the transient displacement function of the piezoelectric diaphragm determined (with ANSYS) was imposed as a prescribed moving-boundary condition to investigate the drop ejection of a printhead (Picojet).

In competitive industrial printing markets, a commercially available piezoelectric DOD ink-jet printhead (Picojet) is known for its enduring reliability, diverse fluid compatibility, and structural durability. This printhead comprises several stainless-steel plates bonded together to form inner flow channels and cavities with ultrasonic bonding, and uses the bending-mode design of a piezoelectric actuator. As a microfluidic dispenser, this printhead is capable of discharging[29,33] up to 18,000 drops/s.

As the preceding review illustrates, most previous work has focused on the influence of the diameter of the nozzle exit, the electrically driven signal, and the properties of the dispensed liquid on the drop ejection of ink-jet printheads. The quality of ink-jet printers is closely related by the volume of a primary drop; the creation of an unwanted secondary drop, known as the satellite drop; and asymmetric drop formation. The primary drop volume determines the resolution of the printed pattern on a substrate or the quantity of microfluidic deposition; however, the occurrence of the satellite drop would disturb the primary drop charging and degrade the printing resolution by impacting the sub-
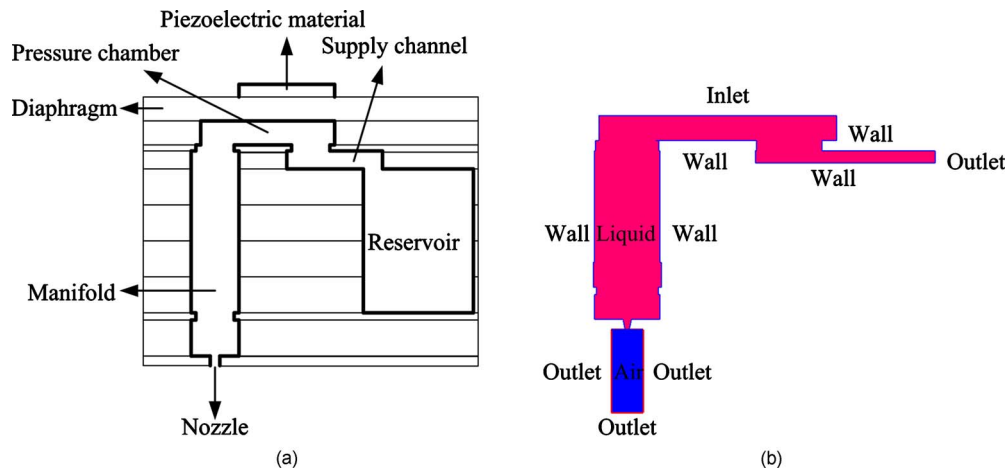
Fig. 1 (a) Schematic of printhead (Picojet) and (b) its computational domain.

strate in undesired locations. The asymmetric drop formation skews the drop trajectory and causes drop misregistration at designated sites, thereby decreasing the accuracy of drop placement. The primary drop volume tends to be affected by the nozzle size and electrically driven signal, and the formation of the satellite drop by the signal waveform and liquid properties. Moreover, the signal waveform and the roundness of nozzle opening seem to have a great effect on the skew phenomenon of drop ejection. In most DOD applications, the voltage waveform that drives the piezoelectric actuator is a square-wave pulse or a succession of two square-wave pulses. The effect of the voltage signal on drop ejection has been investigated experimentally and numerically. From an experimental point of view, authors[34,35] focused mainly on the influence of the maximum amplitude and the frequency of voltage signals on the drop-ejection behavior and on seeking an optimal range of operating conditions in which satellite drops fail to form, based on an iterative method. Because of machine restrictions, the variable range of operation conditions was constrained. In contrast, numerical calculations in research[23,36] focused on a fundamental understanding of the fluid mechanics of DOD ink-jet printing that, in general, involves the elucidation of a competition between the flow directed toward the nozzle outlet and that directed away from it, based on a simplified printhead configuration and an ideally imposed flow rate or pressure pulse as a function of time upstream of the nozzle outlet.

Using numerical simulations we systematically divided a single transducer pulse with a so-called bipolar waveform composed of two square-wave pulses in succession—the first positive and the second negative—into components and investigated the effects of these components and their various combinations on the ejection of a drop in terms of volume, speed, and period of decomposition of the primary drop and the formation of satellite drops. According to Rayleigh's pioneering works,[6] a liquid jet emanating from a nozzle tends to form drops at some distance from the nozzle due to the instability created by the existence of liquid surface tension. This instability leads to the breakup of the liquid jet and then drop formations originate from the growth of an infinitesimal disturbance along the liquid jet,

which reduces the surface area and energy. Following Rayleigh,[6] there is the most rapidly growing disturbance, which sets the sized drops formed under one excitation of external noises and reduces the surface area of the liquid jet the most. The environmental disturbances produced at the nozzle and convected down the jet tend to be random. Therefore, the drop formation frequency and the distance from the nozzle where drops first occur vary randomly. According to previous research,[6,7] the formation of drops can be forced to occur at a well-defined frequency and distance from the nozzle by perturbing the jet periodically with sufficient strength so that random environmental disturbances are ignorable. One method of perturbing the liquid jet periodically is to introduce a periodic pressure variation at the liquid side of the nozzle. In the drop formation of a piezoelectric ink-jet printhead, the pressure variation in the nozzle can be driven by the electrically controlled solid wall movements. This motivates us to investigate the effect of a transducer pulse on the drop formation and microfluidic control of a piezoelectric ink-jet printhead. The results of this work might yield suggestions for the design of ink-jet printheads and contribute to a fundamental understanding of the fluid mechanics of DOD ink-jet printing.

2 Mathematical Models and Computational Methods

We investigated the drop-ejection behaviors of a printhead (Picojet) with the bending-mode design of a piezoelectric actuator.[29,33] We considered a system with an isothermal, incompressible Newtonian fluid of constant density and constant viscosity. The origin of coordinates is based at the center of the nozzle exit plane and the axial unit vector is directed away from the nozzle. Figure 1 shows a schematic of the printhead configuration (Picojet) and its computational domain adopted in our theoretical models. The dimensions of the pressure chamber are a length of 1.880 mm, a width of 0.980 mm, and a height of 0.200 mm, and those of the ink-supply channel are 1.440, 0.550, and 0.100 mm, respectively; the diameter of the nozzle outlet is 0.0343 mm. The dynamics of drop formation are accepted to be governed by the continuity and the

Navier-Stokes equations subject to appropriate boundary and initial conditions. To distinguish the dependent parameters and variables, we made the governing equations, initial conditions, and boundary conditions nondimensional by using the radius of the orifice R_{noz} and capillary period $t_{ca} = (\rho R_{noz}^3 / \sigma)^{1/2}$, in which density ρ and surface tension σ appear as characteristic length and time. Assuming that the fluid obeys the linear Newtonian friction law and neglecting the compressibility, we rewrite these equations in these nondimensional forms:

$$\nabla \cdot \mathbf{v} = 0, \tag{1}$$

$$\frac{1}{Oh}\left(\frac{\partial \mathbf{v}}{\partial \bar{t}} + \mathbf{v} \cdot \nabla \mathbf{v}\right) = \nabla \cdot \left[-\bar{p}\mathbf{l} + \nabla \mathbf{v} + (\nabla \mathbf{v})^T\right] + G\mathbf{k}, \tag{2}$$

in which $\bar{t}$ is time in units of t_{ca}, $\mathbf{v}$ is the fluid velocity vector in units of $U = R_{noz}/t_{ca}$, $\bar{p}$ is static pressure in units of $\mu U / R_{noz}$ with μ denoting the viscosity of the fluid, $\mathbf{l}$ is the identity tensor, $\mathbf{k}$ is gravitational unit vector, $Oh = \mu / \sqrt{\rho R_{noz} \sigma}$ is the Ohnesorge number, and $G = \rho R_{noz}^2 g / \sigma$ is the Bond number with g denoting the gravitational acceleration. Except in a condition of no slip and no penetration at solid walls, the boundary condition for traction at the free surface must be satisfied:

$$n \cdot \left[-\bar{p}\mathbf{l} + \nabla \mathbf{v} + (\nabla \mathbf{v})^T\right] = Oh\, n \, \nabla \cdot n, \tag{3}$$

with the local unit normal vector n at the free surface.

The physical phenomena of drop formation involve a complicated topological variation of the liquid-air interfacial flow such as the liquid decomposition and coalescence. A severe problem confronting researchers in numerical analysis is the mathematical description of the free surface. Possible solutions might arise from either Lagrangian methods or Eulerian methods; the former configure the mesh to adapt continuously to the temporally dependent deformation of the liquid-air interface, whereas the latter employ a fixed mesh through which the arbitrarily shaped interface moves. Although maintaining the discontinuity of the liquid-air interface with fidelity, Lagrangian methods have difficulty treating the severe distortion of a mesh allied to the complicated topological variation of the liquid-air interface. However, the Lagrangian finite-element (FE) method can satisfactorily predict the development of microthreads and overturning but not the dynamics near the point of necking and pinching off.[36] Here, we utilize an interface-capturing method, a variation of the VOF scheme and belonging to the Eulerian type, to resolve this transient behavior of the free surface separating two incompressible and immiscible fluids in the drop formation.[37] The most characteristic feature of this interface-capturing method is that the two fluids are considered as one effective fluid with a scalar variable F, called the volume-fraction function. Let the properties of air and liquid be denoted by subscripts 1 and 2, respectively, and let V_2 and M_2 be the volume and mass of the liquid. Then V_2 and M_2 are given as

$$V_2 = \int F \, dV, \tag{4}$$

$$M_2 = \int F\rho_2 \, dV, \tag{5}$$

in which ρ_2 represents the liquid density. The total volume V is then

$$V = \sum_{K=1}^{2} V_K. \tag{6}$$

Considering mass conservation and constant fluid properties, we obtain an equation for the evolution of the volume fraction:[37,38]

$$\frac{\partial F}{\partial \bar{t}} + \mathbf{v} \cdot \nabla F = 0. \tag{7}$$

By definition, the volume-fraction function is a ratio of volume occupied by the liquid in a computational cell to the total cell volume and takes a unit value at the liquid side and zero at the air side. The crossing region $(0 < F < 1)$ depicts the free surface, of which the position is generally defined to have $F = 0.5$. The critical issue in this method of capturing the free surface is the discretization of the convective term in Eq. (7). We use in particular a multidimensional unsplit advection algorithm with a piecewise construction of a linear interface (PLIC) to make discrete this convective term.[37] In the numerical simulation, the surface tension at the free surface is modeled with a localized volume force f_σ in the framework of the continuum surface force (CSF) model (Brackbill et al.[39]), which is ideally suited for Eulerian interfaces of arbitrary topology:

$$\mathbf{f}_\sigma = \frac{1}{Oh}\left[-\nabla \cdot \left(\frac{\nabla F}{|\nabla F|}\right)\right]\nabla F, \tag{8}$$

where $\mathbf{f}_\sigma$ is the dimensionless counterpart of f_σ and the term in brackets describes the mean curvature of the free surface. This localized volume force can then be incorporated into Navier-Stokes equations. Equation (7) must be coupled with Eqs. (1) and (2). Velocity vectors are first updated on solving Eqs. (1) and (2), then substituted into Eq. (7), so as to obtain the redistribution of the volume-fraction function. The physical properties of the effective fluid including the density and viscosity in each computational cell are determined in the following manner:

$$\rho_e = F\rho_2 + (1-F)\rho_1, \tag{9}$$

$$\mu_e = \frac{F\rho_2\mu_2 + (1-F)\rho_1\mu_1}{\rho_e}. \tag{10}$$

For the model considered here, the arrangement of the types of boundary condition is shown in Fig. 1(b). We suppose that the boundaries at the solid wall meet the conditions of no slip and no penetration. Except for the preceding boundary conditions, the problems with free surface flow also require the conditions at the moving contact line to be specified for a variable level of the wettability of the nozzle wall. The contact line is defined as a location at which liquid, gaseous, and solid phases meet. In the treatment of this wetting condition, we assume that the contact
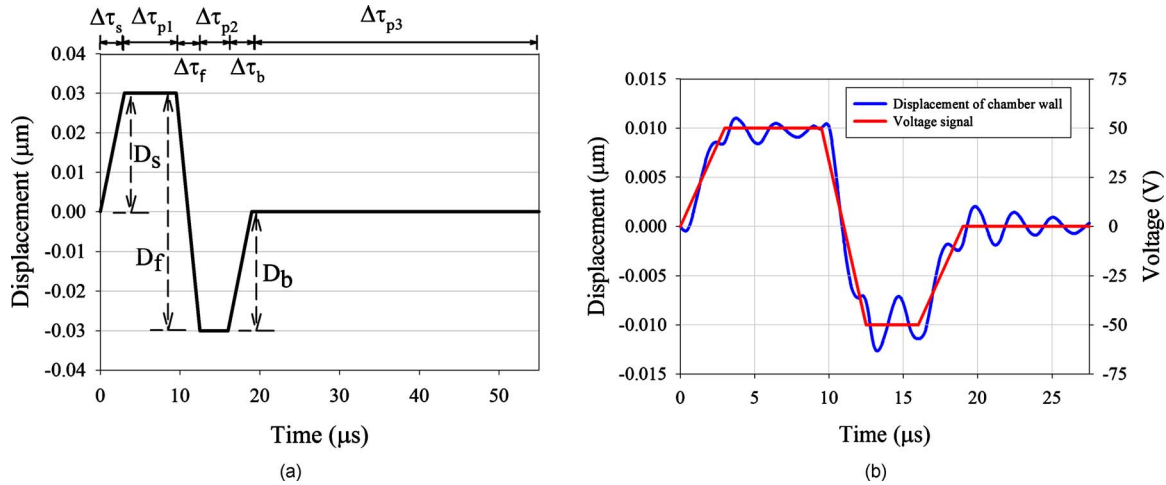
Fig. 2 (a) Temporally dependent function of wall displacement and (b) temporal profile of the voltage signal and displacement of the wall beside the piezoelectric transducer.

angle, formed by the liquid/gas and liquid/solid interface, equals the static (equilibrium) angle according to Young's equation:

$$\sigma \cos \theta_e = \sigma_{sg} - \sigma_{sl}, \quad (11)$$

where θ_e is the static contact angle; and σ, σ_{sg}, and σ_{sl} are the liquid/gas, solid/gas, and solid/liquid interfacial forces, respectively; the related dynamic contact angle on the wall regions is hence set constant during the drop formation. The implementation of the boundary condition for the dynamic contact angle is readily incorporated within the framework of the CSF model. Volumetric force $\mathbf{f}_\sigma$ applied to the numerical cells immediately at the solid walls is calculated with

$$\frac{\nabla F}{|\nabla F|} = n_{wall} \cos \theta_e + \mathbf{t}_{wall} \sin \theta_e, \quad (12)$$

where n_{wall} and $\mathbf{t}_{wall}$ represent outward normal and tangential vectors for the wall, respectively. In this study, the contact angle θ_e is set to be 7.1 deg for the system of water on the plate nickel nozzle wall, according to Yang et al.[29] For the outlet boundaries, the pressure conditions are set to be 1 bar.

The full theoretical model of the piezoelectric DOD inkjet printhead involves the coupling of structural, electric, and interfacial flow fields. The direct coupled-field simulation of this printhead might require substantial computing power and cost. To circumvent the inherent difficulties of this coupled-field simulation, we utilized a temporally dependent function of the wall displacement with a trapezoidal shape and ignored vibration ripples of higher order to model the temporal variation of a deformable diaphragm caused by the bending effect of the piezoelectric material, as shown in Fig. 2(a). The piezoelectric material deflects outward in the period $\Delta\tau_s$ and stays fixed in $\Delta\tau_{p1}$, enlarging the pressure chamber and causing liquid to fill it. In the periods $\Delta\tau_f$ and $\Delta\tau_{p2}$, the piezoelectric material in this so-called forward and pause stages moves inward and keeps still to decrease the chamber volume and cause the liquid to

be ejected from the nozzle outlet. In the periods $\Delta\tau_b$ and $\Delta\tau_{p3}$, the piezoelectric material resumes its equilibrium state, thus producing a negative pressure (suction) to facilitate the pinch-off of liquid thread. In the rest of this paper, we denote supply stage $\Delta\tau_s$, refill stage $\Delta\tau_{p1}$, forward stage $\Delta\tau_f$, pause stage $\Delta\tau_{p2}$, backward stage $\Delta\tau_b$, and equilibrium stage $\Delta\tau_{p3}$. Figure 2(b) shows the temporal variation of the basic voltage signal applied to the piezoelectric transducer (PZT) actuator of a printhead (Picojet) and the wall displacement related to the equilibrium state at the centroid of the chamber wall adjacent to the piezoelectric material. Here, the dimensions of the PZT actuator with rectangular shape are a length of 1.24 mm, a width of 0.98 mm, and a height of 0.2 mm. This momentary displacement function was determined by the stress module of the commercial code (CFD-ACE+) based on the FE numerical method. According to our theoretical models, the drop formation can be driven by a pressure, velocity, or piston moving as a condition at the boundary. Among them, an application of the moving boundary involves the instantaneous remeshing of the interior grids of the solution domains of which the boundaries are moving and thus increases the computational cost. We, therefore, assumed that drop ejection is driven by the boundary condition of specified velocity that is obtained on differentiation of the temporally dependent function of the diaphragm displacement shown in Fig. 2(a). Moreover, the axial deformation of the diaphragm is of the order of 10 nm, much less than the thickness of the ink chamber, 200 μm. Here we neglect the effect of the deformation of the diaphragm adjacent to chamber wall. The rate Q of chamber volume displacement arising from the temporal variation of the deformable diaphragm can be tied with the Weber number, $We \equiv \rho Q^2 / \pi^2 \sigma R_{noz}^3$, which depicts the ratio of inertial to surface tension force.[36] Note that the Weber number can be different in various stages; in the following, except refill, pause, and equilibrium stages in which the corresponding Weber number vanishes, we denote the Weber number in supply stage We_s, forward stage We_f, and backward stage We_b. Therefore, in this study, the temporally dependent function of the diaphragm displace-
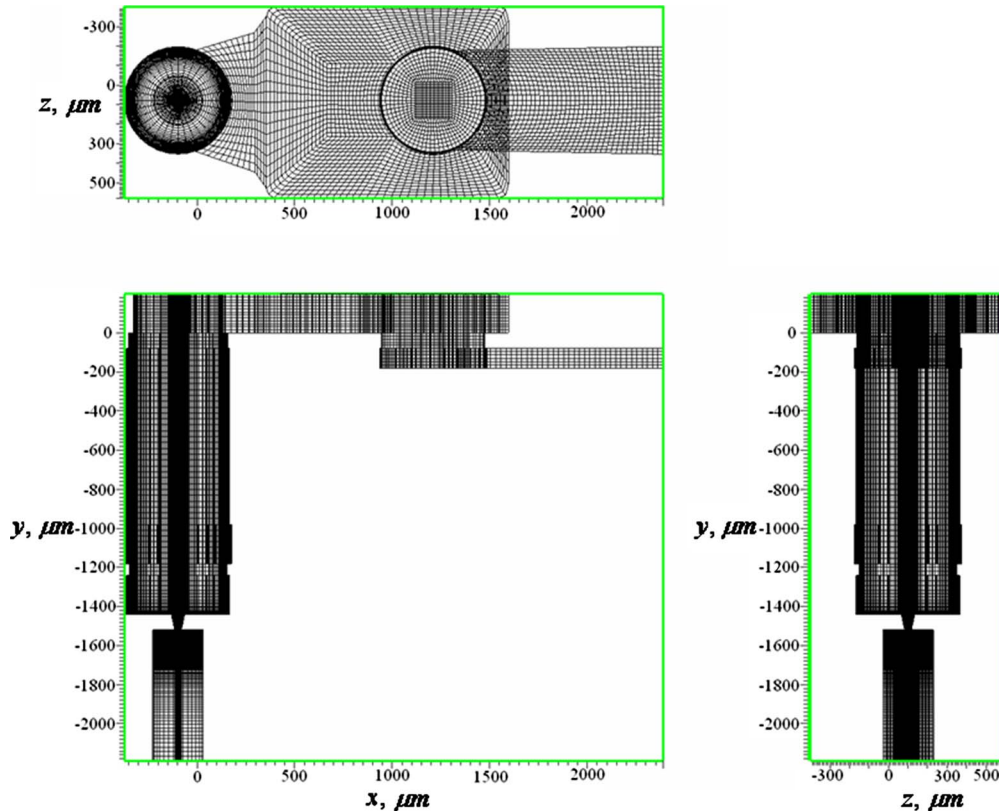
Fig. 3 Numerical grids of a printhead (Picojet).

ment can be represented as the independent parameters: D_s, We_s, $\Delta\tau_{p1}$, D_f, We_f, $\Delta\tau_{p2}$, D_b, We_b, and $\Delta\tau_{p3}$ for the waveform in Fig. 2(a).

To validate the present theoretical models, we performed all computations with multipurpose commercial code (CFD-ACE+) based on the finite-volume numerical method to solve the 3-D Navier-Stokes equations and the iterative semi-implicit method for pressure-linked equations consistent (SIMPLEC) with velocity-pressure coupling. Diffusion fluxes are approximated by central differences. Here, the explicitly first-order backward Euler scheme served for discretization of time. The primary variables are the velocity, pressure, and volume fraction, which cannot be determined until convergent criteria are satisfied for each time step. Due to the use of the multidimensional unsplit advection algorithm, which is a geometrically based flux calculation procedure for the evolution of volume-fraction function, an inherent stability requirement on the size of the time step must be considered. To decrease simulation time without interfering with stability, the size of the next time step is computed before every new time step. The time step is calculated for a fixed value of the Courant number (Co) and the variable local velocity in the interface cells and their immediate neighbors ($0 < F < 1$). Corresponding to the maximum velocity $u_{i,\max}$ found in the grid cells of interest, the minimum value of the time step is calculated and implemented using the following relationship:

$$\Delta t_{\text{new}} = \text{Co}\frac{\Delta y_{\min}}{u_{i,\max}}, \tag{13}$$

where Δt_{new} is the time step calculated, and $\Delta y_{\min}$ is the length scale of the smallest grid cells of interest. The Co number is utilized to a restrict the crossing of interface to a certain amount of a cell width during each time step. In this study, the value of the Courant number is set as low as 0.05 to ensure that the free surface crosses less than a cell during the time step. Therefore, the actual local Courant number is less than or equal to 0.05. In an early stage of this study, test cases with Co=0.05 and 0.02 were also performed. The influence of the finer time step size on the transient behavior of drop ejection is insignificant. Considering most applications of ink-jet printing, we use a fluid of density 1000 kg m^{-3}, viscosity 3.5 cp, and surface tension 0.0725 N m^{-1} at which Ohnesorge number equals the value 0.1. In addition, based on the preliminary simulations, we choose the values of D_s=0.03 μm, $\Delta\tau_s$=3 μs, $\Delta\tau_{p1}$=9 μs, D_f=0.06 μm, $\Delta\tau_f$=3 μs, $\Delta\tau_{p2}$=3.5 μs, D_b=0.03 μm, and $\Delta\tau_b$=3 μs as the reference conditions of the transducer pulse in the remainder of this study unless they are indicated otherwise. Here, the value of $\Delta\tau_{p3}$ is adjusted to ensure that the flow in the printhead is gradually stopped with the initial condition reload for the next drop ejection.

Table 1 Interval for a liquid thread from a nozzle outlet to pinch off, with three meshes.

186,898 cells	282,408 cells	411,654 cells
	Period to Pinch Off (μs)	
30.512	30.512	30.515

Table 3 Primary drop volume with three meshes.

	186,898 cells	282,408 cells	411,654 cells
Time (μs)		Primary Drop Volume (pL)	
30.5	8.94073	8.93109	9.081
40	6.89494	7.34343	7.45479

3 Simulation Results

3.1 Grid Convergence and Model Validation

The numerical grids of the printhead to simulate drop ejection are illustrated in Fig. 3. The computational domain is divided into five parts—the ink-supply channel, the ink chamber, the manifold, the nozzle, and the area outside the nozzle. To achieve a uniform distribution of the discretization errors, we utilized nonuniform grids that adopt a small grid spacing in regions such as near the nozzle, the immediate solid walls, and the trajectory of the flight drops of which the derivatives of the variables alter radically and large discretization errors are expected. All numerical grids are 3-D hexagons with a smallest spacing of 1.5 μm, which corresponds to the criterion that, according to the VOF method, at least four to five cells are required across the gap to provide an adequate resolution of the free surface in that gap.[37,38]

To test the grid dependence, we devised grids of total numbers 186,898, 282,408 and 411,654 cells adding 10% of the total grid points in each dimension. Tables 1–3 show the time at which the liquid thread pinches off from the nozzle outlet, the drop tip position, and the velocity of the drop head defined as a estimated velocity at the leading edge of the drop, as well as the volume of the primary drop using varied meshes. In this present study, the shape of the primary drop after the oscillation of the surface wave is sufficiently decayed by viscous dissipation could be approximated to a sphere whose diameter is determined by measuring the maximum end-to-end distance of the liquid drop and could be used to estimate the drop volume. It is shown that the pinch-off times obtained with these three
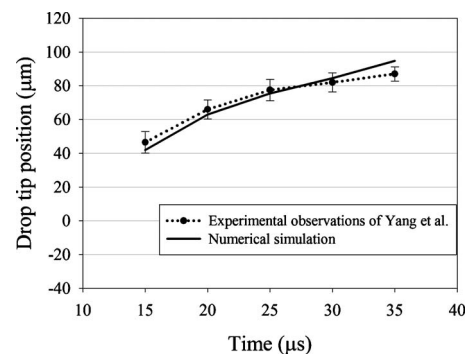
meshes are in excellent agreement. Table 2 shows the difference in drop tip position where the velocity of drop head is estimated decreases with grid refinement. It is seen that the discretization error in drop tip position is around 0.43% when refining from 282,408 to 411,654 cells, whereas it is 1.04% when refining from 186,898 to 282,408 cells. In addition, Table 2 also presents that the discretization error in the estimated velocity of the drop head is around 2.28% between 282,408 and 411,654 cells, and that it is around 3.78% between 186,898 and 282,408 cells. Table 3 makes clear that the difference in primary drop volume decreases with grid refinement. The computed error in drop volume at 40 μs when the shape of the primary drop could be approximated to a sphere between 282,408 and 411,654 cells is around 1.49%, and that between 186,898 and 282,408 cells is around 6.11%. The net volumes of fluid expelling from the nozzle outlet over the total time period of simulation are 19.9982 pL on 186,898 grids, 19.5928 pL on 282,408 grids, and 19.6372 pL on 411,654 grids. The difference in this net volume of fluid between 282,408 and 411,654 cells is 0.226% and that between 186,898 and 282,408 cells 2.07%. Therefore, grid independence is satisfied with a mesh of 282,408 cells, achieving a compromise between accuracy and computing time, which in this paper is around 96 h of central processing unit (CPU) time. As also illustrated in existing literature,[40] note that when the primary drop moves downstream behind a certain simulation field, it does not conserve mass well. This may be due to the numerical grids with larger spacing arranged in this field and/or the linear order of the multidimensional unsplit advection algorithm with PLIC. The most effective remedy may be a careful attention to higher order schemes and sufficient grid resolutions. Figure 4 shows a comparison of the predictions with experimental observations of Yang et

Table 2 Velocity of the drop head with three meshes.

	186,898 cells	282,408 cells	411,654 cells
Time (μs)	Head Velocity (m s^{-1}) [Drop Tip Position (μm)]		
15	5.81632 (46.3)	5.59234 (45.9)	5.66525 (46)
20	4.00525 (70.7)	4.15712 (69.7)	4.20037 (70.3)
25	2.97289 (87.8)	2.93412 (87.1)	2.83467 (87.1)
30.5	2.74526 (103.1)	2.75629 (101.9)	2.72694 (102.5)
35	3.09152 (116)	3.19418 (114.9)	3.25551 (115.8)
40	2.84138 (131.3)	2.58049 (130)	2.46021 (130.1)

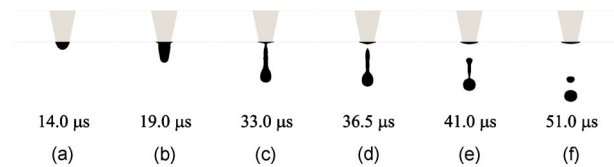**Fig. 4** Comparison between experiment and numerical simulation.

Fig. 5 Key stages observed in our numerical experiment 4: (a) ejection, (b) stretching, (c) necking, (d) pinching off, (e) recoil, and (f) breaking up.

al.[29] of the temporal evolution of the position of the leading edge of the liquid drop. In this case, we used water as a working fluid whose density, viscosity, and surface tension are 1000 kg m^{-3}, 1.0 cp, and 0.0725 N m^{-1}, respectively. The corresponding parameters of the transducer pulse were set to be D_s=0.029 μm, $\Delta\tau_s$=3 μs, $\Delta\tau_{p1}$=6.5 μs, D_f=0.058 μm, $\Delta\tau_f$=3 μs, $\Delta\tau_{p2}$=3.5 μs, D_b=0.029 μm, and $\Delta\tau_b$=3 μs. In addition, we excluded the first drop ejection from data analysis owing to an unbalanced liquid meniscus at the nozzle exit plane. Restricted to the limit of experimental setup configured by Yang et al.,[29] the drop tip position was measured every 5 μs after the liquid thread emerged from nozzle outlet. This temporal resolution is insufficient to determine the evolution of ejected liquid during different stages of a piezoelectric actuator. However, based on the results shown in Fig. 4, the numerical models predict the same trend as the experimental observation, and a reasonable agreement is obtained between the experiment and simulation. In addition, the comparison between the predictions and visualized images of evolution of ejected drop could be found in research of Yang et al.,[29] which used the theoretical models and arrangements of numerical grids similar to those used in this study.

3.2 Forward Stage

According to research of Dong et al.,[16] a typical DOD drop formation is divisible typically into six stages—ejection, stretching, necking, pinching off, recoil, and breaking up. Figure 5 shows these key stages observed in our numerical simulations. In the ejection stage, the liquid meniscus initially protrudes from the nozzle orifice and then quickly extends outward due to the forward stroke of the piezoelec-

tric actuator [Fig. 5(a)]. As the forward actuation ends, the rate of liquid flow toward the plane of the nozzle exit rapidly decreases during the period $\Delta\tau_{p2}$; then some liquid is even sucked back into the nozzle under the effect of the backward actuator. A decreased rate of liquid flow toward the nozzle outlet would cause the difference in axial velocity between the head of the liquid column and liquid near the plane of the nozzle exit. This velocity inequality accounts further for the stretching of the liquid column, as shown in Fig. 5(b). In addition, two necking points are observable during the stretching stage, first near the nozzle orifice and second near the bulbous head of liquid thread, as shown in Fig. 5(c). After a short interval, the tail of liquid thread pinches off from the nozzle outlet to form a freely flying liquid thread [Fig. 5(d)]. The tail and the leading edge of the freely flying liquid thread are asymmetric and thus behave differently. Because the pressure at pinching off is large, the tail of the free liquid thread begins to recoil toward the thread head and gradually evolves into a bulbous shape, as shown in Fig. 5(e). During the recoil stage, the second necking point continues to develop until the freely flying liquid thread breaks into two parts—a primary drop and a secondary freely flying liquid thread with asymmetric ends. Because the secondary freely flying liquid thread retracts to the decrease of the surface energy, a satellite drop might be formed [Fig. 5(f)]. This DOD drop formation with one satellite drop formed by end pinching might be found in most current simulations. In addition, two specific times could be observed in the drop formation process just described: pinching-off time when the ejected liquid thread detaches from the remaining liquid in the nozzle and breaking-up time when the primary drop is formed.

To investigate the effect of D_f, $\Delta\tau_f$, and We$_f$ on drop ejection, we conducted seven numerical experiments, as shown in Table 4. It is noticed that not all waveforms designed may assure the actuator of returning to the original position after the backward stokes are applied. This is so because to systematically examine the effects of components of a transducer pulse, all parameters are fixed except the one of interest in a numerical experiment. The disruptions of the fluid interface failed to occur in experiment 2,

Table 4 List of experiments for the forward stage.

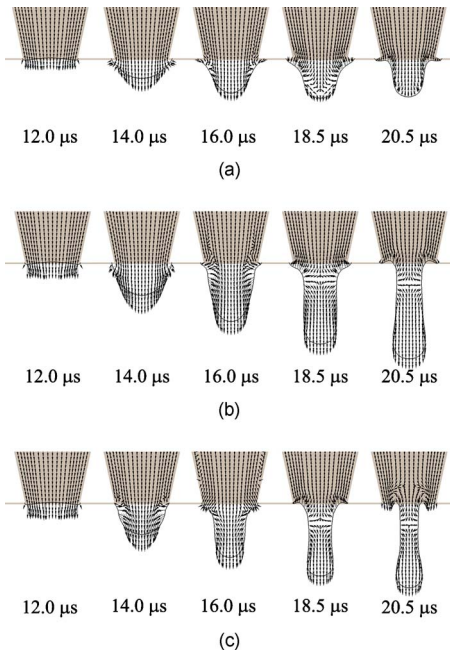| Experiment	D_s (μm)	$\Delta\tau_s$ (μs)	$\Delta\tau_{p1}$ (μs)	D_f (μm)	$\Delta\tau_f$ (μs)	We$_f$	$\Delta\tau_{p2}$ (μs)	D_b (μm)	$\Delta\tau_b$ (μs)
1	0.03	3	9	0.06	3	162.7	3.5	0.03	3
2	0.03	3	9	0.03	3	40.7	3.5	0.03	3
3	0.03	3	9	0.03	1.5	162.7	3.5	0.03	3
4	0.03	3	9	0.12	6	162.7	3.5	0.03	3
5	0.03	3	9	0.06	1.5	650.7	3.5	0.03	3
6	0.03	3	9	0.03	0.75	650.7	3.5	0.03	3
7	0.03	3	9	0.12	4.8	254.2	3.5	0.03	3

Fig. 6 Evolution of the liquid thread shape and velocity vector at the liquid side in experiments (a) 2, (b) 1, and (c) 3.

whereas experiment 1 with D_f increased to 0.06 μm and experiment 3 with $\Delta\tau_f$ decreased to 1.5 μs produced a pinching off of the liquid thread. It would appear that the ratio of D_f to $\Delta\tau_f$ must exceed a minimum value for a successful drop ejection. The value of $D_f/\Delta\tau_f$ multiplied by the area of the chamber wall adjacent to the piezoelectric material represents the rate of chamber volume displacement and could be related to the Weber number (inertial/surface tension force). For experiments 1, 2, and 3, Fig. 6 shows the evolution of the liquid thread shape and velocity vector in the liquid side. On the effect of the backward stroke of actuation, the flow near the plane of the nozzle exit is reversed, which causes the formation of a stagnation plane sweeping toward the head of liquid thread. Figure 6(a) shows that, under the conditions of experiment 2, the stagnation plane sweeps through the entire liquid thread and the thread fails to pinch off. Experiments 1 and 3, in contrast, show that the stagnation plane does not sweep to the liquid thread tip and the effect of the reversed flow causes necking near the nozzle and then the pinching off of the liquid thread, as shown in Figs. 6(b) and 6(c). Figure 7(a) shows the variation of the volume of the primary drop in these conditions. The drop volume in experiment 1 equals approximately that in experiment 5, and the drop volume in experiment 3 that in experiment 6; the drop vol-
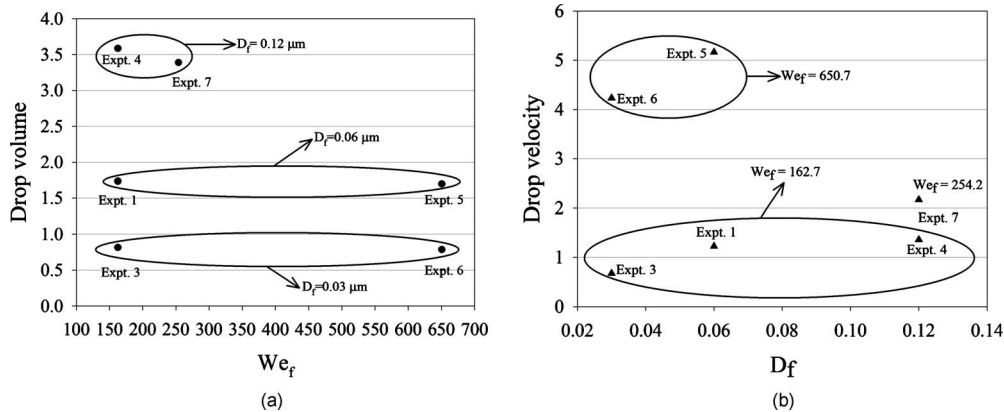

Fig. 7 Variation of (a) the volume of the primary drop and (b) the velocity of the primary drop in experiments; the volume is in units of R_{noz}^3 =5.044 pL and the velocity in units of R_{noz}/t_{ca}=2.056 m s^{-1}.
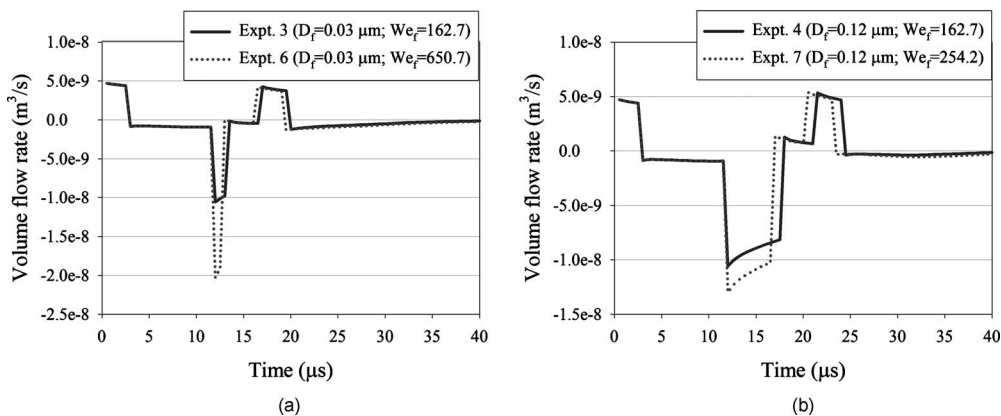

Fig. 8 Temporal variation of the rate of volume flow at the plane of the nozzle entrance in (a) experiments 3 and 6 and (b) experiments 4 and 7.
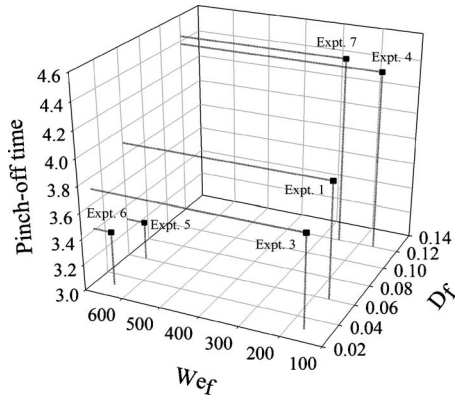
Fig. 9 Variation with experiments of pinch-off time of liquid thread from nozzle exit; the time is in units of $t_{ca} = 8.341$ μs.

ume in experiment 4 is near that in experiment 7. The drop volume falls into three zones that correspond to three distinguishable values of D_f. Figure 7(b) shows the variation of the velocity of the center of mass of the primary drop on breaking up in these cases. The velocity of the primary drop increases substantially as We_f is increased, which corresponds to an increased inertial force. Experiments 1, 3, and 4 show that the drop velocity correlates positively with the primary drop volume; a similar relation is seen at different value of We_f, as shown in experiments 5 and 6 in agreement with the results of Feng.[23] This is so because the large amount of ejected liquid decreases the restoring effect of surface tension due to the smaller curvature of the fluid interface. Figure 8 shows the temporal variation of the rate of volume flow at the plane of the nozzle entrance. The total volume entering the nozzle during the forward stroke of the actuation in experiment 3 and representing the area underneath the line in Fig. 8(a) is 15.268 pL, whereas that in experiment 6 is 19.725 pL. Figure 8(b) shows that the total volume entering the nozzle during the forward actuation in experiment 7 is greater than that in experiment 4. These results indicate that through conservation of mass, the total volume ejected from the nozzle increases when the value of We_f increases and that of D_f remains constant. The variation with experiments of duration of the liquid thread pinching off from the nozzle outlet is shown in Fig. 9. The period for pinching off in experiment 3 is less than that in experiments 1 and 4. The period to pinch off seems to

increase as D_f increases with We_f remaining constant; a possible explanation is that the large amount of ejected liquid corresponding to a large value of D_f decreases the effect of driving the breaking of surface tension by the small curvature of the fluid interface. As already mentioned, however, the large ejected volume of liquid might weaken the restoring effect of surface tension and then result in a large forward momentum density, which facilitates the pinching off of liquid thread with a rapid elongation and necking, as shown in Fig. 7(b). When We_f has a large value, the forward momentum density because of increased volume of ejected liquid increases greatly, as shown in Fig. 7(b). The period to pinch off in experiment 5 is less than that in experiment 6 as the driving effect on pinching off through the increasing forward momentum density induced by increasing D_f is dominant, as shown in Fig. 9. Figure 9 also shows that the period for pinching off of the liquid thread in experiment 5 is less than that experiment 1. When We_f increases, the forward momentum density possibly increases, which accelerates the pinch-off of liquid thread by rapid elongation and necking, shown in Fig. 7(b). A similar relation is found between experiments 3 and 6. However, Fig. 8 shows that, when the value of We_f increases, the ejected liquid volume increases, thus decreasing the effect of the driving of the breaking of surface tension and then decelerating the thread pinching off. Figure 9 shows that the period for pinching off in experiment 7 is greater than that in experiment 4 because the driving of the pinching off is contained by the increased volume of ejected liquid when We_f in experiment 7 is greater than that in experiment 4.

3.3 Backward Stage

Table 5 shows the variation of the conditions of the backward stroke in five numerical experiments for the investigation of the effect of D_b, $\Delta \tau_b$, and We_b on the drop ejection. Figure 10 shows the variation of the volume of the primary drop and the velocity of the center of mass of the primary drop upon breaking up in these experiments; the drop volumes are approximately constant in all cases. Moreover, the estimated values of the drop velocity in all experimental conditions fall into the same range. The backward inertial force in all these cases might be insufficient to draw all ejected liquid back and the meniscus would invade the tube through conservation of mass. Figure 11 shows the evolution of the shape of the liquid thread during the period

Table 5 List of experiments for the backward stage.

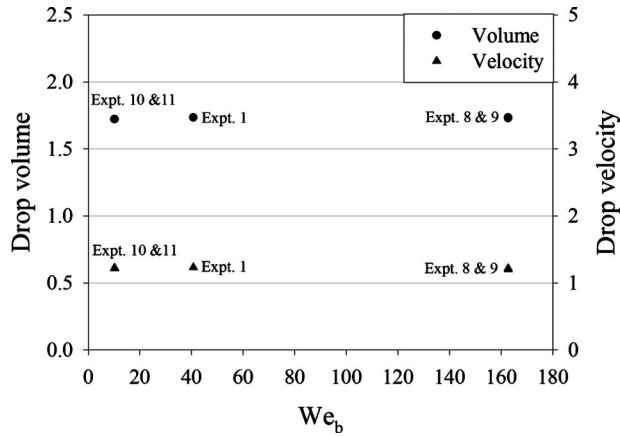| Experiment	D_s (μm)	$\Delta \tau_s$ (μs)	$\Delta \tau_{p1}$ (μs)	D_f (μm)	$\Delta \tau_f$ (μs)	$\Delta \tau_{p2}$ (μs)	D_b (μm)	$\Delta \tau_b$ (μs)	We_b
1	0.03	3	9	0.06	3	3.5	0.03	3	40.7
8	0.03	3	9	0.06	3	3.5	0.06	3	162.7
9	0.03	3	9	0.06	3	3.5	0.03	1.5	162.7
10	0.03	3	9	0.06	3	3.5	0.03	6	10.2
11	0.03	3	9	0.06	3	3.5	0.06	12	10.2

Fig. 10 Variation of the volume of the primary drop and velocity of the primary drop in experiments; the volume is in units of R_{noz}^3 =5.044 pL and the velocity in units of R_{noz}/t_{ca}=2.056 m s^{-1}.

of the backward stroke in the various experiments. The temporal variation of the tip position of the liquid thread for these cases is almost constant, and the contours of the liquid interface are similar, except near the plane of the nozzle exit. Under the effect of the reversed flow caused by the backward actuation, the liquid interface near the plane of the nozzle exit tends to be drawn back, and the mean curvature of the interface is negative and becomes smaller and smaller (liquid surface near the nozzle exit is concave). Here, we assume that the principal curvature on the free surface is positive if the center of the circle of curvature lies on the liquid side. According to Eq. (8), the smaller the mean curvature at a point on the free surface, the larger the

localized volume force induced by surface tension effect. After the period of the backward actuation terminates, the liquid in the nozzle would thus be pulled out again through the effect of the imbalance of surface tension and the inertia of the liquid in the ink-supply channel. The extent of tube invasion by the retracting meniscus and the acceleration of the thinning of the fluid neck increase as We$_b$ increases (see Fig. 11, 18.5 and 19.5 μs). Experiment 8, in which the condition of the backward actuation has the same value of We$_b$ as in experiment 9 but a large working interval $\Delta\tau_b$ shows a greater extent of tube invasion and a smaller curvature of the liquid interface, thus causing a larger rate of volume flow of the liquid toward the nozzle outlet. Figure 12 shows the temporal variation of the rate of volume flow at the plane of the nozzle entrance. At the end of the backward stroke, the rate of volume flow at the plane of the nozzle entrance is directed toward the nozzle outlet and turns gradually into a still state. As already mentioned, experiment 8 has the rate of volume flow much less than experiment 9 because of the small curvature of the retracting meniscus. Experiment 11 is analogously expected to have a lesser rate of volume flow than experiment 10, as shown in Fig. 12. Figure 13 shows the variation with experiments of duration of the liquid thread pinching off from the nozzle exit. Experiment 11 seems to have the smallest interval of pinching off. The backward actuation of experiment 11 might proceed through a considerable period in which pinching off of the liquid thread occurs before the rate of volume flow of the liquid toward the nozzle outlet begins because the surface tension is unbalanced. Experiment 8 appears to have large duration of pinching off because the large rate of volume flow toward the nozzle outlet occurs behind the period of the backward stroke, as shown
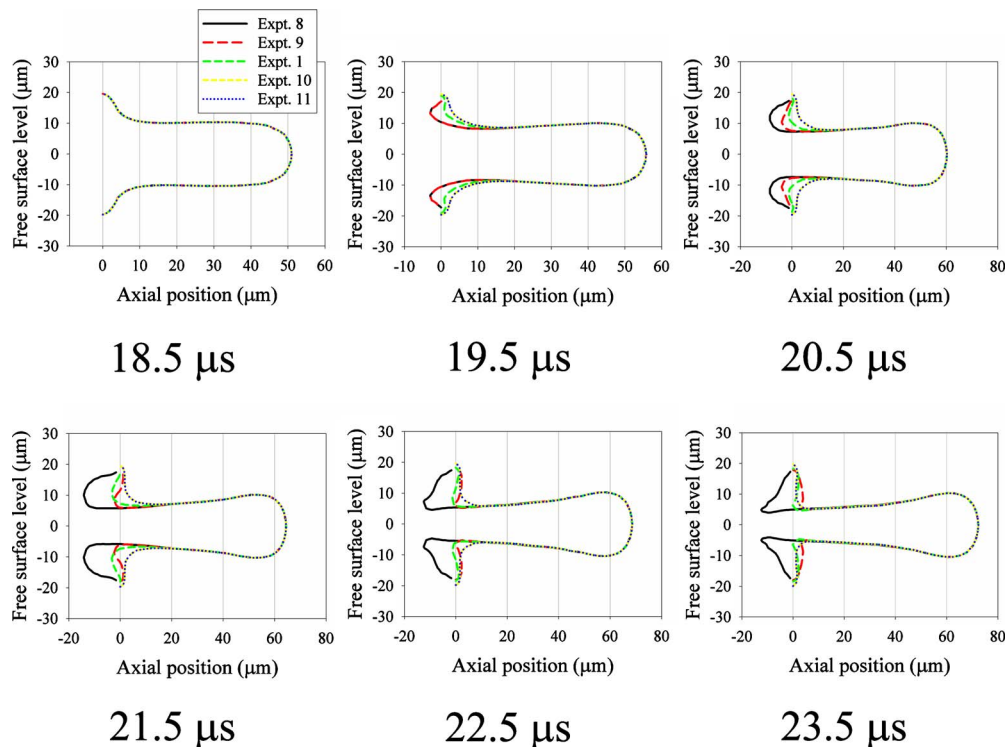

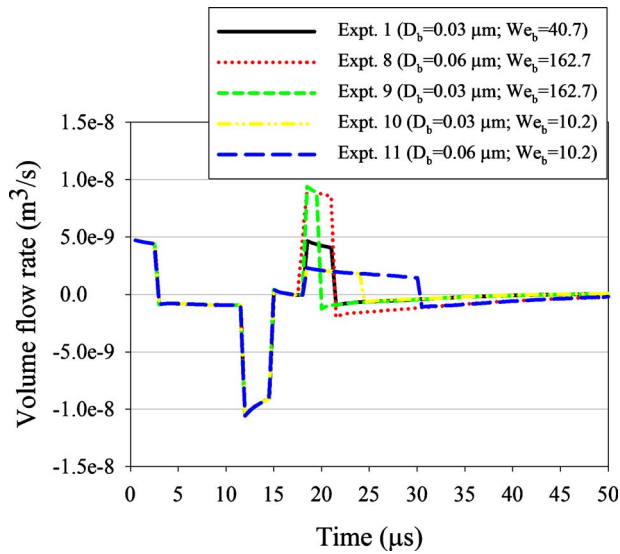**Fig. 11** Evolution of the shape of the liquid thread during the backward stroke.

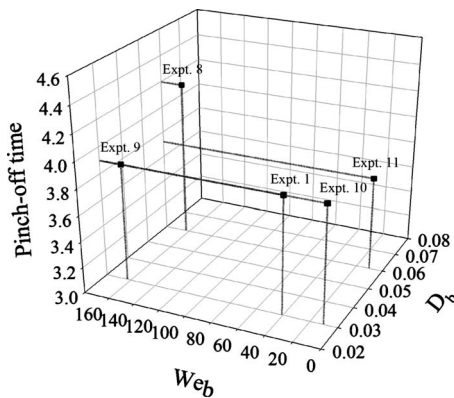**Fig. 12** Temporal variation of the rate of volume flow.

Fig. 13 Variation with experiments of pinch-off time of liquid thread from nozzle exit; the time is in units of $t_{ca} = 8.341$ μs.

in Fig. 12, therefore decelerating the thinning of the fluid neck and prolonging the pinching off. Distinct values of We_b cause varied acceleration of the thinning of the fluid neck, which facilitates the thread pinching off. Various intervals $\Delta \tau_b$ of backward stoke along with various values of We_b may cause varied extent of tube invasion, which obstructs the thread pinching off by inducing the rate of volume flow toward the nozzle outlet beyond the period of backward actuation. Experiments 1, 9, and 10 with different combinations of We_b and $\Delta \tau_b$ lead to the same duration of the thread pinching off, as shown in Fig. 13.

3.4 Pause Stage

In an investigation of the effect of $\Delta \tau_{p2}$ on the ejection of a drop, Table 6 summarizes nine numerical experiments with various values of $\Delta \tau_{p2}$. Figures 14 and 15 show the temporal evolution of the shape of the liquid thread near the point of pinching off for experiments 1 and 12 and 8 and 15, respectively. After pinching off of the liquid thread occurs, experiment 12 shows that the tail of the freely flying liquid thread recoils toward the thread head, whereas experiment 1 shows one satellite drop to be formed by end pinching. Both experiments 8 and 15 show one satellite drop to be formed, but in the case of experiment 15, the satellite drop flies with a larger velocity than that of the former primary drop; the satellite drop might overtake and then merge with the primary drop. Among cases considered here, in experiments 12, 13, 16, and 17 there occurs no satellite drop. These results indicate that a decrease in $\Delta \tau_{p2}$ can damp the formation of the satellite drop; further investigations are described in the next section. Figure 16 shows the variation of the volume of the primary drop and the velocity of the center of mass of the primary drop upon breaking up in considered experiments. The volume of the drop is approximately constant in all cases except experiments 12, 13, 16, and 17 with slightly larger drops. Moreover, other than experiments 12, 13, 16, and 17 with slightly larger drop velocities, all experiments show nearly the same estimated velocity. The tail of the free liquid thread might tend to

Table 6 List of experiments for the pause stage.

Experiment	D_s (μm)	$\Delta \tau_s$ (μs)	$\Delta \tau_{p1}$ (μs)	D_f (μm)	$\Delta \tau_f$ (μs)	$\Delta \tau_{p2}$ (μs)	D_b (μm)	$\Delta \tau_b$ (μs)
1	0.03	3	9	0.06	3	3.5	0.03	3
12	0.03	3	9	0.06	3	1.75	0.03	3
13	0.03	3	9	0.06	3	0.8	0.03	3
8	0.03	3	9	0.06	3	3.5	0.06	3
14	0.03	3	9	0.06	3	1.75	0.06	3
15	0.03	3	9	0.06	3	0.8	0.06	3
9	0.03	3	9	0.06	3	3.5	0.03	1.5
16	0.03	3	9	0.06	3	1.75	0.03	1.5
17	0.03	3	9	0.06	3	0.8	0.03	1.5

31.5 μs   33.5 μs   37.5 μs   45.0 μs

(a)

31.5 μs   33.5 μs   37.5 μs   45.0 μs

(b)

Fig. 14 Temporal evolution of the liquid thread shape in experiments (a) 1 and (b) 12.

31.5 μs   36.5 μs   39.0 μs   50.0 μs
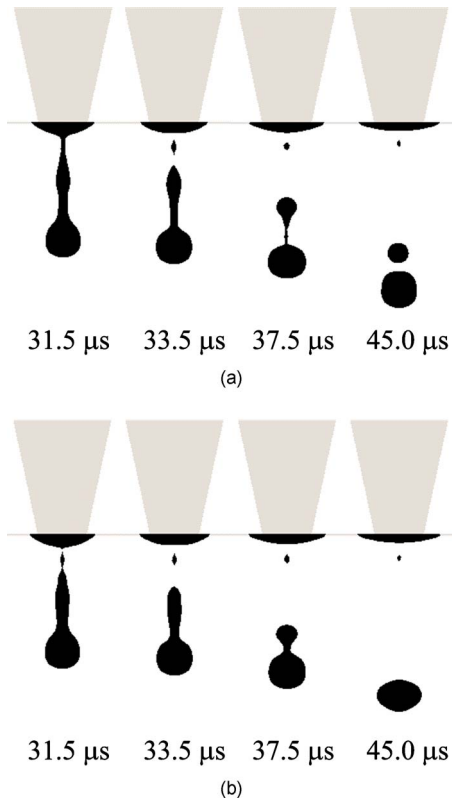
(a)

31.5 μs   36.5 μs   39.0 μs   50.0 μs

(b)

Fig. 15 Temporal evolution of the liquid thread shape in experiments (a) 8 and (b) 15.

recoil toward the thread head, thus causing an increased volume and velocity of the drop. Figure 17 shows the variation with experiments of duration of the liquid thread pinching off from the nozzle exit. This duration decreases with decreasing $\Delta\tau_{p2}$. For a decreasing period in which the flow rate toward nozzle outlet is reversed, the necking and then pinching off of the liquid thread from the nozzle outlet occurs early. Figure 18 shows the temporal evolution of the free surface contour of the liquid thread crossing the period of actuation of the backward stroke for experiments 1, 12, and 13. Compared to experiment 1, experiments 12 and 13 show an early necking of the liquid thread, because of the decreased pause stage. The temporal variation of the position of the thread head for these experiments is almost constant, as shown in Fig. 18.

3.5 Suppression of Satellite Drops

The breaking up of freely flying liquid thread has two modes—multiple breaking up because of wavelike instability and end pinching, where the liquid thread pinches off from a bulbous end.[16,41] The mechanism of end pinching may be a consequence of the fluid motion induced by capillary pressure gradients near the end of liquid thread.[41] The two modes of the breaking up of the free liquid thread could be observed in the presented simulations. The examples of end pinching and multiple breaking up are found in Figs. 5 and 19, respectively. During multiple breaking up, a wavelike disturbance appears along the freely flying liquid thread. This disturbance grows until the liquid thread
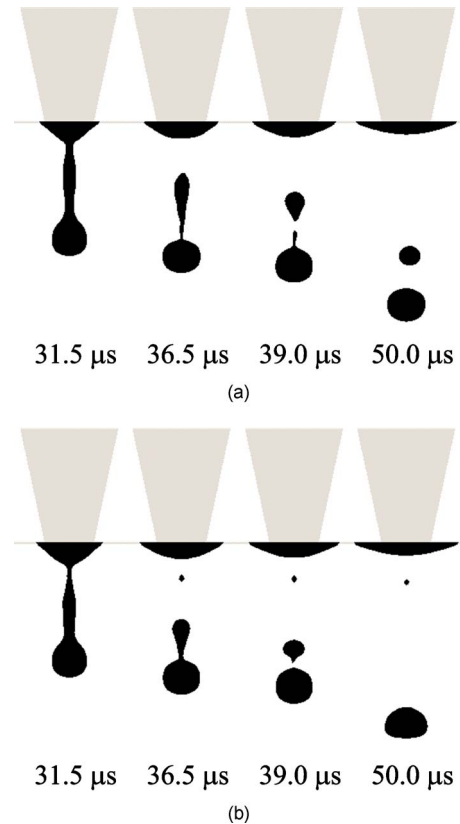
breaks up at several places and varied times. The liquid thread in multiple breaking up tends to form numerous satellite drops of varied size.

The breaking up of the freely flying liquid thread is related closely to the length of the liquid thread at pinching off, which is defined as the distance between the leading-edge position and tail-tip position of the thread. In their DOD dispensing experiments Dong et al.[16] observed that, for the freely flying water thread of small length at pinching off, the formation of a satellite results from end pinching
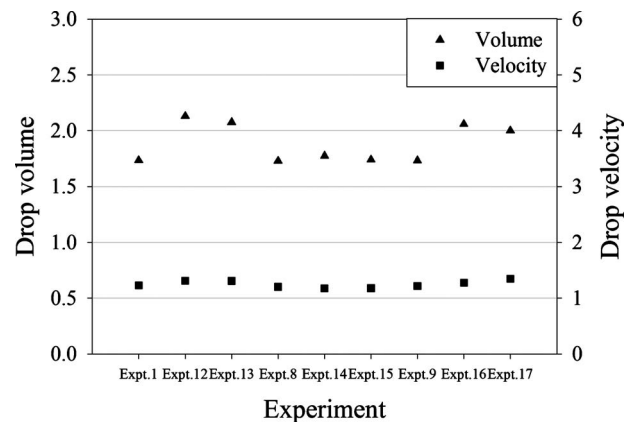

Fig. 16 Variation of the volume of the primary drop and velocity of the primary drop in experiments; the volume is in units of R_{noz}^3 $=5.044$ pL and the velocity in units of $R_{noz}/t_{ca}=2.056$ m s^{-1}.
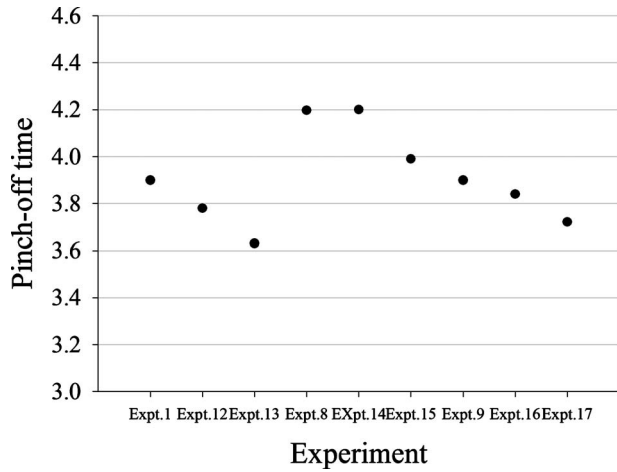
Fig. 17 Variation of duration of the liquid thread pinching off from nozzle exit; the time is in units of $t_{ca}=8.341$ μs.

24.0 µs   30.0 µs   36.0 µs   38.0 µs   42.0 µs

Fig. 19 Satellite formation by multiple breaking up observed in numerical experiment 6.

and for a long thread, a wavelike instability occurs and multiple breaking up is dominant. Figure 20 shows the variation with cases of liquid thread length at pinching off in the current simulations. For a ratio of thread length to nozzle radius (17.15 μm) greater than about 9.67, multiple breaking up occurs through a wavelike instability. When this ratio is smaller than 8.8, the breaking up becomes an end-pinching mode, as shown in Fig. 20(a). In addition, the longer the length of liquid thread, the more satellite drops are formed. Experiment 5, for example, shows five satellite drops, experiment 6 three satellite drops, and experiment 7 two satellite drops. The thread length at pinching off is positively correlated with the value of We_f. With the same
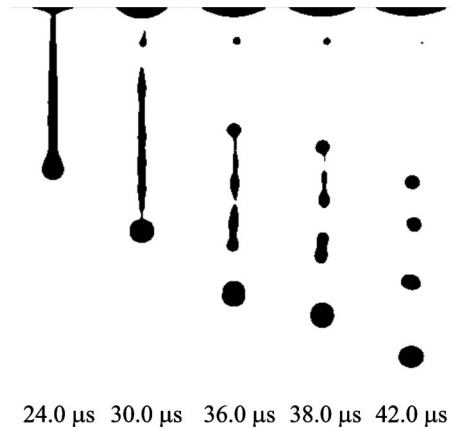
value of We_f, an increased D_f might yield an increased length of thread at pinching off. The causes of these phenomena might be that, when We_f increases, the forward momentum density increases, thus accounting for an increasing difference in axial velocity and then a more elongated thread. When We_f is constant, the larger D_f implies a larger forward momentum density and then greater elongation of the thread. A decreased $\Delta\tau_{p2}$ could slightly shorten the liquid thread length at pinching off by accelerating the rate of necking, shown in Fig. 20(b).

To investigate further the effect of actuation conditions on the thread length at pinching off, we performed additional experiments, as illustrated in Table 7. Figure 21 shows the variation in liquid thread length at pinching off for these experiments. The values of l_b/R_{noz} in these cases
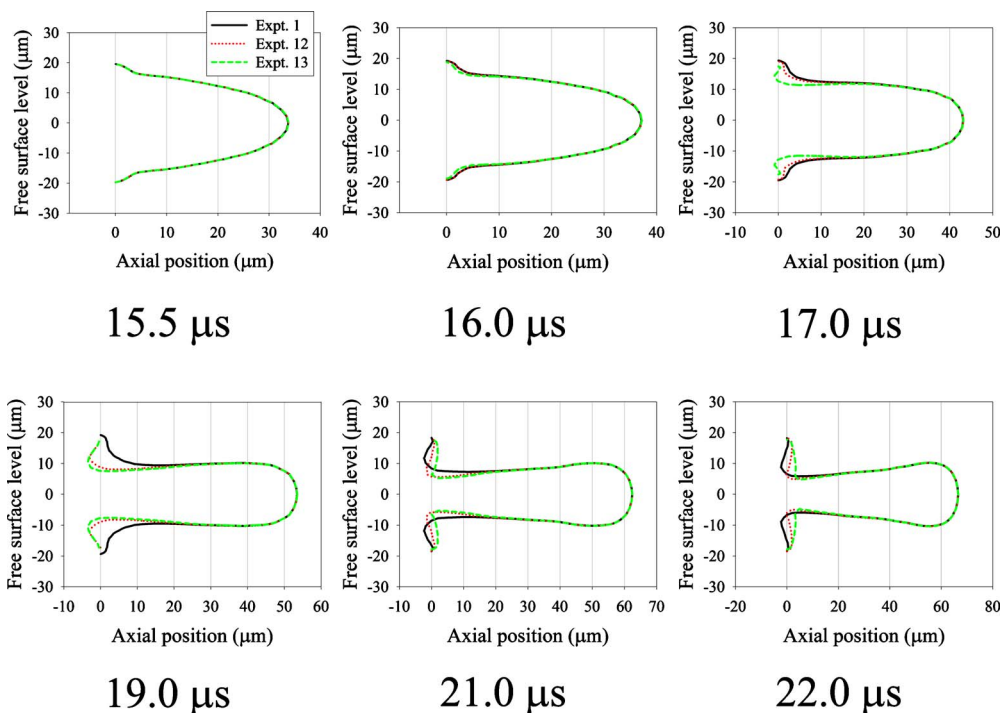

Fig. 18 Temporal evolution of the free surface contour of the liquid thread crossing the period of actuation of the backward stroke.
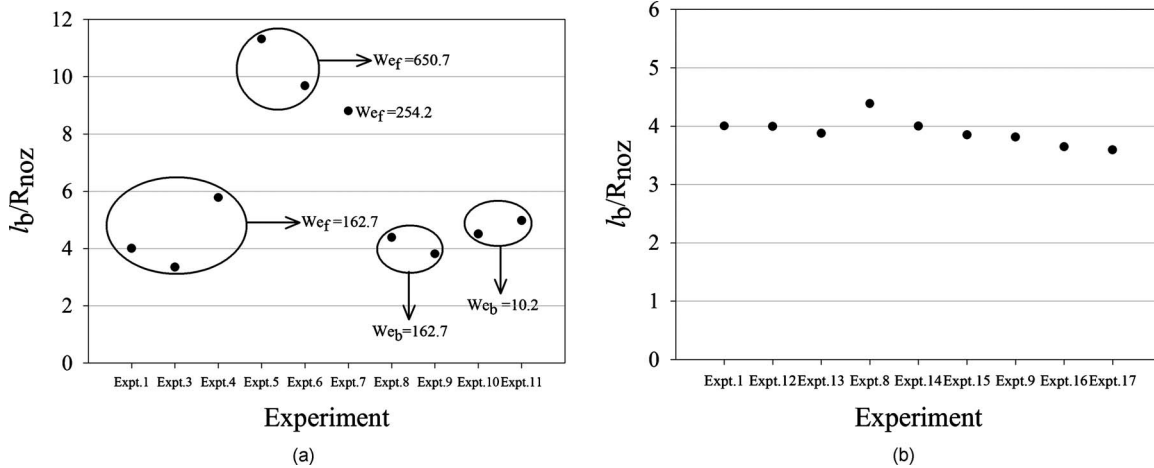
Fig. 20 Variation of length of the liquid thread at pinching off with varied conditions in (a) the forward and backward stages and (b) the pause stage.

are all above 9.67; the multiple breaking-up mode is then dominant. These results indicate that the varying parameters in the pause and backward stages cause a slight variation of thread length at pinching off. From the preceding discussion, we conclude that the thread length at pinching off from the nozzle outlet is governed mainly by the conditions of the forward stroke—D_f and We_f.

In most applications, the satellite drops would degrade the printing quality or increase the difficulty of a precise microfludic control; for this reason, a suppression of satellite drops has considerable practical significance. As already noted, the breaking-up mode of the freely flying liquid thread and its thread length at pinching off have been shown to be mutually positively correlated. In the end-pinching mode, the formation of a satellite drop seems to be predictable and its size is comparable. Several authors[16,42–44] have suggested criteria to observe satellite formation by end pinching; for instance, the numerical research done by Notz and Basaran[43] shows that the liquid thread with sufficiently large initial aspect ratio defined as the ratio of a half thread length to thread radius pinched off daughter drops from almost spherical ends by end pinching when $Oh < O(0.1)$. In this study, the shape of the liquid thread was assumed to be a cylinder with hemispherical

caps at its two ends. In contrast, satellite drops caused by multiple breaking up tend to occur arbitrarily and have varied size.

To investigate the suppression of satellite drops, we focus our attention on the end-pinching breaking up of the freely flying liquid thread into the primary drop and the free secondary liquid thread. This secondary thread contracts into a single satellite drop. In the following analysis based on work of Dong et al.,[16] we denote the pinching-off time as t_{b1}, the breaking-up time as t_{b2}, the thread length at pinching off as l_b, the position as z_t of the tail tip of the thread, the position z_p of the leading edge of the thread, the average speed $v_r = \mathrm{d}z_t/\mathrm{d}t\|_{t_{b2} \to t_{b1}}$ of the retreating thread tail, and average speed $v_p = \mathrm{d}z_p/\mathrm{d}t\|_{t_{b2} \to t_{b1}}$ of the leading edge of the thread, as indicated schematically in Fig. 22. The freely flying liquid thread would contract into a single drop without satellite formation provided that the thread length at pinching off from the nozzle is less than a critical value l_b^*. If we denote the radius of this final single drop as r_d,

$$l_b - 2r_d \leqslant (t_{b2} - t_{b1})(v_r - v_p). \tag{14}$$

Scaling the period with the capillary time and the velocity with the capillary speed, we obtain

Table 7 List of additional experiments.

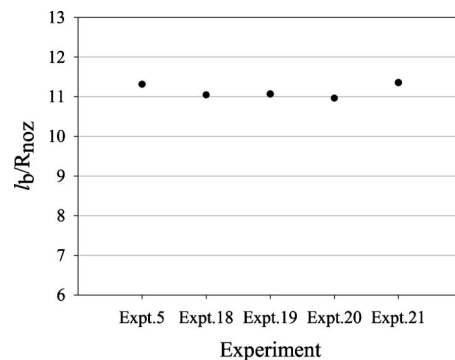| Experiment	D_s (μm)	$\Delta\tau_s$ (μs)	$\Delta\tau_{p1}$ (μs)	D_f (μm)	$\Delta\tau_f$ (μs)	$\Delta\tau_{p2}$ (μs)	D_b (μm)	$\Delta\tau_b$ (μs)
5	0.03	3	9	0.06	1.5	3.5	0.03	3
18	0.03	3	9	0.06	1.5	0.8	0.03	3
19	0.03	3	9	0.06	1.5	0.8	0.03	1.5
20	0.03	3	9	0.06	1.5	0.8	0.03	0.75
21	0.03	3	9	0.06	1.5	0	0.12	3

Fig. 21 Variation of length of liquid thread at pinching off in various conditions.
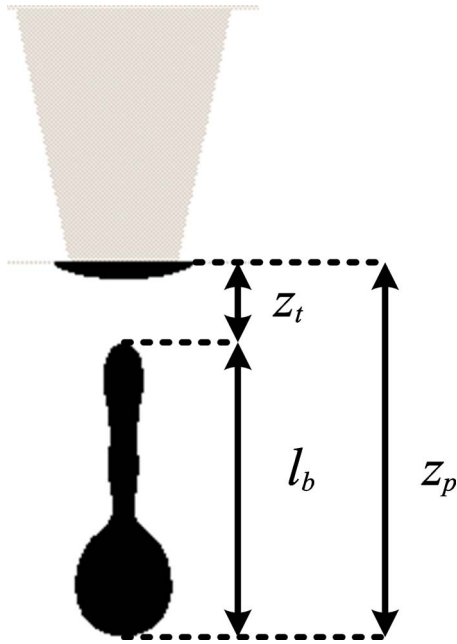
Fig. 22 Schematic diagram of representative points during the evolution of an ejected liquid thread.

$$t_{b1} = c_1 t_{ca}, \tag{15}$$

$$t_{b2} = c_2 t_{ca}, \tag{16}$$

$$v_r = a v_{ca}, \tag{17}$$

in which c_1, c_2, and a are parameters, $t_{ca} = (\rho R_{noz}^3 / \sigma)^{1/2}$ is the capillary duration, and $v_{ca} = (\sigma / \rho R_{noz})^{1/2}$ is the capillary speed. By definition, c_1 is the ratio of pinching-off time t_{b1} to the capillary duration, c_2 is the ratio of breaking-up time to the capillary duration, and a is the ratio of retreating velocity to the capillary speed. In this study, the time scale is $t_{ca} \approx 8.341$ μs and velocity scale $v_{ca} \approx 2.056$ m s^{-1}. Sub-

stituting Eqs. (15)–(17) into Eq. (14), we rewrite the equation as

$$l_b - 2r_d \leqslant (c_2 - c_1) t_{ca} v_{ca} a \left(1 - \frac{v_p}{v_r} \right). \tag{18}$$

Replacing r_d with the radius of nozzle orifice and assuming that $v_r > v_p$, we rearrange Eq. (18) as

$$\frac{l_b}{R_{noz}} < (c_2 - c_1)a + 2 \equiv \frac{l_b^*}{R_{noz}}. \tag{19}$$

Table 8 presents this prediction in our simulations. Except for experiment 15, l_b / R_{noz} is larger than the critical value l_b^* / R_{noz}; then one satellite drop can be observed. Notice that although the value l_b / R_{noz} in experiment 15 is less than the critical value l_b^* / R_{noz}, the prediction in this case shows one satellite formed; however, the lifetime of this satellite is quite short compared to experiment 8, as shown in Fig. 15. One explanation for this is that to highlight the significant variables of the critical value l_b^* / R_{noz}, we approximate the radius of the final single drop r_d as nozzle radius and neglect the term v_p / v_r in Eq. (18), which would slightly enlarge the upper limits l_b^* / R_{noz}. We can see in Table 8 that the ratio of the radius r_p of the primary drop followed by one satellite-to-nozzle radius (17.15 μm) in experiment 15 is approximately 0.746, which can be expected to be slightly smaller than r_d / R_{noz}. From Eq. (19), the critical length of the thread at pinching off without formation of satellite drops depends mainly on c_2, c_1, and a. The value c_2 represents the time at which the primary drop is formed through either end pinching or multiple breaking up. As recommended by Dong et al.,[16] c_1 and c_2 are closely related to the liquid properties, nozzle radius, and the waveform of the transducer pulse. The variation of c_2 in our current experiments is given in Fig. 23 and Table 8. In experiment 1, c_2 is approximately equal to that in experiment 5 and c_2 in experiment 3 to that in experiment 6. The value c_2 in experiment 4 is almost the same as that in experiment 7.

Table 8 Liquid thread length at pinch-off compared with prediction.

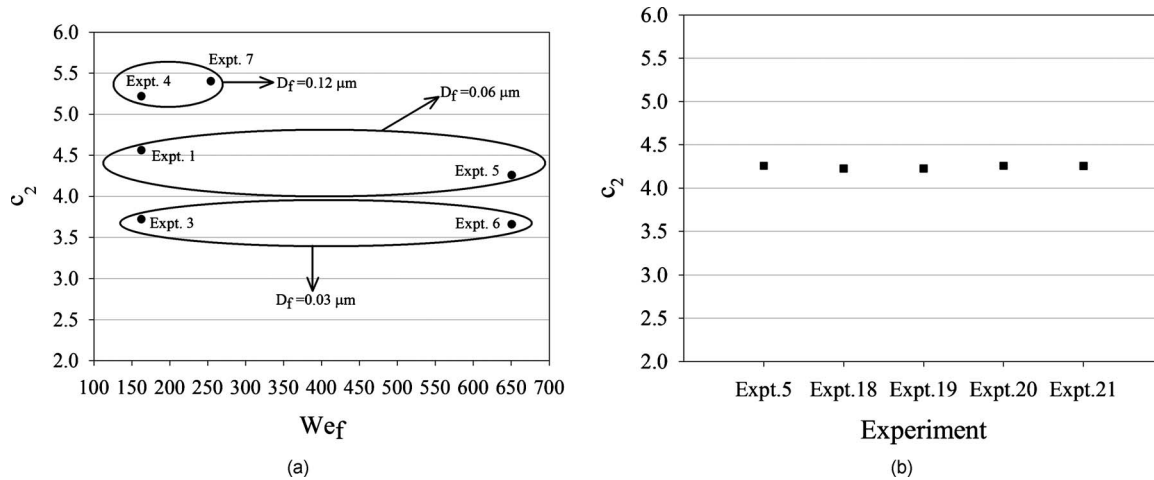| Experiment	C_1	C_2	a	v_{ca} (m s^{-1})	v_p (m s^{-1})	r_p / R_{noz}	l_b / R_{noz}	l_b^* / R_{noz}
1	3.899	4.559	2.635	2.056	2.38	0.745	4.0	3.739
4	4.378	5.217	2.501	2.056	2.443	0.949	5.773	4.099
8	4.197	4.617	2.721	2.056	2.511	0.745	4.385	3.143
9	3.899	4.498	2.833	2.056	2.4	0.745	3.813	3.698
10	3.898	4.858	2.259	2.056	2.56	0.744	4.501	4.169
11	3.719	4.859	2.298	2.056	2.546	0.744	4.974	4.618
14	4.2	4.62	3.263	2.056	2.426	0.751	4.0	3.371
15	3.99	4.65	3.004	2.056	2.433	0.746	3.848	3.983

Fig. 23 Variation of c_2 with experiments shown in Tables (a) 4 and (b) 7.

These results indicate that c_2 depends strongly on D_f. The relation between c_1 and the waveform of the transducer pulse is shown in preceding sections. Compared to the experimental results of Dong et al.,[16] the ratio of the average speed of the retreating thread tail to the capillary speed, as shown in Table 8, ranges from 2.2 to 3.2 showing reasonable values. Note that in a few simulation cases, upon the pinching off of the liquid thread from the nozzle outlet, a tiny isolated liquid fragment called flotsam is observed. This flotsam is characterized by the vanishing velocity and size comparable to a single numerical cell. The appearance of the flotsam would interfere with the measurement of the retreating speed and the length of liquid thread at pinching off, and should be excluded from the data analysis. As already noted, experiments 12, 13, 16, and 17 appear to show no satellite drop because the tail of the liquid thread contracts into the thread head. Experiments 12 and 13 show an interval t_{b1} of pinching off smaller than in experiment 1. To estimate the critical value of experiments 12 and 13, we took $c_2=4.559$ and $a=2.635$, as obtained in experiment 1 with the same value of D_f, and because the value of a in experiments 14 and 15 is larger than that in experiment 8, as indicated in Table 8. We thus obtain the critical thread length at pinching off $l_b^*/R_{noz}=4.055$, larger than $l_b/R_{noz}=3.994$ in experiment 12, in agreement with a prediction obtained from Eq. (19). An estimate of the value l_b^*/R_{noz} in experiments 16 and 17 is similarly obtained on taking c_2

and a identical to values in experiment 9. Table 9 contains the estimate of a critical thread length l_b^*/R_{noz} in experiments 12, 13, 16, and 17. It is seen that a decrease in pause stage $\Delta\tau_{p2}$ could both shorten the liquid thread length l_b at pinching off and enlarge the critical value l_b^*, thus damping the satellite formation.

Based on the analysis above and from Eq. (19), we prefer the larger c_2, the smaller c_1, and the larger a to induce the larger l_b^*/R_{noz}. The larger the value l_b^*/R_{noz}, the wider the range of liquid thread length at pinching off without satellite formation. As shown in Figs. 23 and 9, both c_1 and c_2 appear to increase when D_f increases with constant We_f. An increase in We_f leads to a decrease in c_1 when D_f is fixed, as shown in Fig. 9. However, the larger We_f would cause the longer length l_b/R_{noz} of liquid thread at pinching off, which may contribute to the formation of satellite drops, as depicted in Fig. 20. Both l_b/R_{noz} and c_1 tend to decrease as the pause stage $\Delta\tau_{p2}$ decreases. According to research of Dong et al.,[16] the interval between c_1 and c_2 increases when liquid viscosity increases, liquid surface tension decreases, or nozzle radius decreases. The parameter a is shown not to be significantly related to the liquid surface tension, nozzle radius, and the waveform of the transducer pulse. However, as the liquid viscosity increases, the value of a would slightly increase. In conclusion, for a DOD drop generator with a given liquid, the

Table 9 Estimate of the critical value of the thread length at pinching off.

Experiment	C_1	C_2	t_{ca} (μs)	a	v_{ca} (m s^{-1})	l_b/R_{noz}	l_b^*/R_{noz}
12	3.78	4.559	8.341	2.635	2.056	3.994	4.055
13	3.63	4.559	8.341	2.635	2.056	3.878	4.449
16	3.84	4.498	8.341	2.833	2.056	3.644	3.869
17	3.721	4.498	8.341	2.833	2.056	3.592	4.206

Table 10 List of experiments for the supply stage.

Experiment	D_s (μm)	$\Delta \tau_s$ (μs)	We_s
22	0.03	3	40.7
23	0.06	3	162.7
24	0.03	1.5	162.7
25	0.03	6	10.2
26	0.06	12	10.2

Fig. 25 Temporal variation of the rate of volume flow rate at the plane of the nozzle entrance.

waveform of transducer pulse could carefully be designed to obtain a longer t_{b2}, a shorter t_{b1}, and then larger upper limits l_b^*.

3.6 Supply, Refill, and Equilibrium Stages

To investigate the effect of D_s, $\Delta \tau_s$, and We_s on the liquid supply to the printhead, we performed five numerical experiments, shown in Table 10. Figure 24 shows the temporal variation of the position of the free surface along the center line of the nozzle in these cases. Upon initiation of the liquid supply, the flow in the nozzle and ink supply channel is directed toward the ink chamber having a volume displacement caused by the altered dimensions of the piezoelectric actuator. Under the effect of the reversed flow, the meniscus near the nozzle outlet retracts and the mean curvature of the interface is negative and becomes smaller and smaller (liquid surface is concave). After the termination of supply, the flow in the nozzle turns to the nozzle outlet through the effect of the imbalance of surface tension and inertia of the liquid in the supply channel in this so-called refill stage. According to the position of the free surface as a function of time shown in Fig. 24, the rate of the retracting meniscus increases as We_s increases. Experiment 26 reveals that, after 6 μs, the rate of the retracting meniscus decreases. The inertial force of the reversed flow

Fig. 24 Temporal variation of the position of the free surface along the center line of the nozzle.

is gradually balanced by the restoring effect of the surface tension due to the smaller and smaller curvature of the liquid interface. Except for experiment 23, all numerical experiments show that the extent of invasion of the tube by the retracting meniscus is about 15 μm from the nozzle outlet. Moreover, Fig. 24 also shows that the period of the refill stage, which ends when the free surface along the nozzle center line reaches the nozzle exit plane, is approximately 9 μs in these cases. Figure 25 shows the temporal variation of the rate of volume flow at the plane of the nozzle entrance. The rate of reversed volume flow increases as We_s increases. After termination of the ink supply, experiment 23 has a rate of volume flow less than experiment 24, whereas experiment 26 has a rate of volume flow less than experiment 25. The large extent of tube invasion caused by the retracting meniscus might account for the small curvature of the liquid interface, and then the larger restoring effect of surface tension to drive the flow toward the plane of the exit nozzle at the termination of ink supply.

In most applications of microfluidic control, firing frequency, which represents the number of drops per second the printhead can dispense, determines the throughput or the speed at which an ink jet system can complete images. The firing frequency of printheads is equal to the reciprocal of the total time interval of a transducer pulse. In current study, the equilibrium stage $\Delta \tau_{p3}$ forms a large proportion of the transducer pulse and then its value determines the firing frequency of the printhead. To obtain stable drop formation, the value of $\Delta \tau_{p3}$ should be large enough to ensure the flow in the printhead of reverting to the initial condition for the next drop ejection. Figure 26 shows the variation of the primary drop volume and velocity with firing frequency by varying the value of $\Delta \tau_{p3}$ in experiment 1. Both variation of drop volume and velocity are around 1% at a frequency of 4.348 kHz. When the firing frequency increases to 15.625 kHz, the discrepancy of drop volume is still below 10%, yet the drop velocity is as large as 21.6%. From the results shown in Fig. 26, the firing frequency below 5 kHz appears to confirm the stable drop formation.

4 Conclusions

We conducted numerical simulations to investigate the effect of actuation conditions on the drop ejection of a printhead (Picojet) of DOD type that is commercially available.
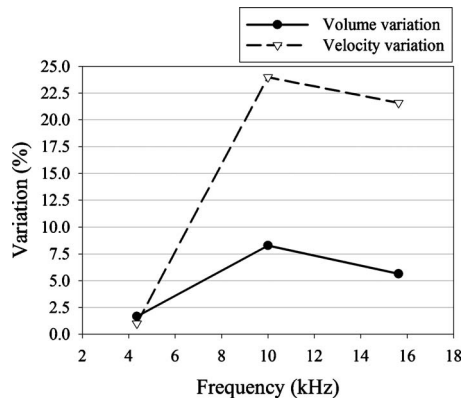
Fig. 26 Variation of the primary drop volume and velocity with firing frequency.

According to numerical results of the FE simulation, the temporary displacement function of the piezoelectric diaphragm displays a trapezoidal shape with higher-order vibration ignored and is divisible into six stages—supply, refill, forward, pause, backward, and equilibrium. The fluid is assumed to be an isothermal, incompressible Newtonian fluid of constant physical properties—density and viscosity. The dynamics of the drop ejection are governed by these independent parameters: We_s, We_f, We_b, D_s, D_f, D_b, $\Delta\tau_{p1}$, $\Delta\tau_{p2}$, and Ohnesorge number Oh, in which We represents Weber number; D is the maximum displacement of the piezoelectric diaphragm; $\Delta\tau$ is the duration of the different stages of a single transducer pulse; and the subscripts s, f, b, $p1$, and $p2$ depict supply, forward, backward, refill, and pause stages, respectively.

For the investigation of the forward stage, the flow inertia, i.e., We_f, must be large enough that a DOD drop can be formed in accordance with intuition. The simulations also show that the volume of the primary drop increases as D_f increases. These results are consistent with the fact that the larger is the volume displacement of the ink chamber, the larger is the volume of liquid ejected from the DOD nozzle. Increasing We_f might produce an increased velocity of the primary drop. The drop velocity slightly increases when the volume of the ejected drop increases. This result is explicable on assuming that an increased volume of the ejected drop might cause a decreased curvature of the liquid interface, thus accounting for the decreased restoring effect of surface tension.

From the investigation of the backward stage, the velocity and the volume of the primary drop seem to depend weakly on the varied conditions of the backward stroke. The extent of tube invasion by the retracting meniscus is closely related to We_b and $\Delta\tau_b$. From the investigation of the pause stage, the velocity and the volume of the primary drop remain constant but the formation of the satellite drops tends to be suppressed as $\Delta\tau_{p2}$ decreases. There is a strong possibility that decreasing $\Delta\tau_{p2}$ might decrease the length l_b of the liquid thread at pinching off and increase the upper limit l_b^* for the free thread length without satellite formation. This maximum limit l_b^* depends strongly on the time t_{b1} at which the liquid thread pinches off from nozzle outlet, time t_{b2} at which the free liquid thread breaks up into primary drop and secondary liquid thread, and the av-

erage speed v_r of the retreating thread tail. Moreover, the pinch-off time t_{b1} and breakup time t_{b2} are shown to be significantly associated with the waveform of the transducer pulse.

Based on the nondimensional analysis of the system parameters and variables in the presented theoretical models, the effect of liquid viscosity can be related to Ohnesorge number $Oh = \mu/\sqrt{\rho R_{noz}\sigma}$, which measures the important of viscous force relative to surface tension force. Several studies[16,23,29,36] have examined the relationship between Ohnesorge number and DOD drop formation. Despite using different DOD generators, both numerical and experimental results in these studies show similar conclusions: as Oh increases with constant actuation conditions, the pinching-off and breaking-up time of the ejected liquid increase slightly, while both the liquid thread length at pinching off and primary drop volume decrease slightly. In addition, a drop ejected at larger values of Oh tends to move at a slower speed. In some cases, with a larger Oh, drop breakup may not occur and more powerful actuation is required. The major goals of this paper were to investigate the effects of a single transducer pulse on the DOD drop formation at a specified Oh value. The readers are referred to good literature[16,23,29,36] for a full discussion about the effect of Oh on DOD drop formation.

The most popular application of ink-jet printheads is to print digital data onto a medium at high resolution. The drop size should hence be as small as practicable, but an ink-jet printhead designed to deliver a small drop size for high resolution undergoes a severe restriction of throughput for an application at poor resolution. A reliable approach to decrease the drop size for one case but not others should hence extend the applicable areas of the specific ink-jet printhead. A prospectively unique capability of piezoelectric printheads is modulation of the drop size with a single transducer pulse having complicated positive and negative parts to manipulate the fluid motion in the nozzle. The results of this work might yield physical insight into the components of the transducer pulse and lead to the development of modulation of the drop size in piezoelectric DOD ink-jet printheads.

References

1. J. F. Dijksman and A. Pierik, "Fluid dynamical analysis of the distribution of ink jet printed biomolecules in microarray substrates for genotyping applications," *Biomicrofluidics* **2**(4), 044101 (2008).
2. Y. Do Kim, J. P. Kim, O. S. Kwon, and I. H. Cho, "The synthesis and application of thermally stable dyes for ink-jet printed LCD color filters," *Dyes Pigm.* **81**(1), 45–52 (2009).
3. T. Shimoda, K. Morii, S. Seki, and H. Kiguchi, "Inkjet printing of light-emitting polymer displays," *MRS Bull.* **28**(11), 821–827 (2003).
4. B. A. Ridley, B. Nivi, and J. M. Jacobson, "All-inorganic field effect transistors fabricated by printing," *Science* **286**(5440), 746–749 (1999).

5. M. Komatsu, Y. Murayama, and H. Hashimoto, "Protein fragment imaging using ink jet printing digestion technique," *Appl. Surf. Sci.* **255**, 1162–1164 (2008).
6. L. Rayleigh, "On the stability of liquid jets," *Proc. London Math. Soc.* **10**, 4–13 (1879).
7. J. Eggers, "Nonlinear dynamics and breakup of free-surface flows," *Rev. Mod. Phys.* **69**(3), 865–929 (1997).
8. S. F. Pond, *Inkjet Technology and Product Development Strategies*, Torrey Pines Research, Carlsbad, CA (2000).
9. R. R. Allen, J. D. Meyer, and W. R. Knight, "Thermodynamics and hydrodynamics of thermal ink jets," *Hewlett-Packard J.* **36**(5), 21–27 (1985).
10. Y. Wang and J. Bolkor, "Ultra-high-resolution monolithic thermal bubble inkjet print head," *J. Micro/Nanolith. MEMS MOEMS* **6**(4), 043009 (2007).
11. P. H. Chen, W. C. Chen, and S. H. Chang, "Bubble growth and ink ejection process of a thermal ink jet printhead," *Int. J. Mech. Sci.* **39**(6), 683–695 (1997).
12. K. C. Fan, J. Y. Chen, C. H. Wang, and W. C. Pan, "Development of a drop-on-demand droplet generator for one-drop-fill technology," *Sens. Actuators, A* **147**(2), 649–655 (2008).
13. K. S. Kwon, "Speed measurement of ink droplet by using edge detection techniques," *Measurement* **42**(1), 44–50 (2009).
14. C. D. Meinhart and H. S. Zhang, "The flow structure inside a microfabricated inkjet printhead," *J. Microelectromech. Syst.* **9**(1), 67–75 (2000).
15. T. W. Shield, D. B. Bogy, and F. E. Talke, "Drop formation by DOD ink-jet nozzles: a comparison of experiment and numerical simulation," *IBM J. Res. Dev.* **31**(1), 96–110 (1987).
16. H. M. Dong, W. W. Carr, and J. F. Morris, "An experimental study of drop-on-demand drop formation," *Phys. Fluids* **18**(7), 072102 (2006).
17. A. Asai, "Three-dimensional calculation of bubble growth and drop ejection in a bubble jet printer," *ASME Trans. J. Fluids Eng.* **114**(4), 638–641 (1992).
18. A. Asai, T. Hara, and I. Endo, "One-dimensional model of bubble growth and liquid flow in bubble jet printers," *Jpn. J. Appl. Phys., Part 1* **26**(10), 1794–1801 (1987).
19. P. H. Chen, H. Y. Peng, H. Y. Liu, S. L. Chang, T. I. Wu, and C. H. Cheng, "Pressure response and droplet ejection of a piezoelectric inkjet printhead," *Int. J. Mech. Sci.* **41**(2), 235–248 (1999).
20. J. E. Fromm, "Numerical calculation of the fluid dynamics of drop-on-demand jets," *IBM J. Res. Dev.* **28**(3), 322–333 (1984).
21. W. T. Pimbley, "Drop formation from a liquid jet: a linear one-dimensional analysis considered as a boundary value problem," *IBM J. Res. Dev.* **20**(2), 148–156 (1976).
22. C. W. Hirt and B. D. Nichols, "Volume of fluid (VOF) method for the dynamics of free boundaries," *J. Comput. Phys.* **39**(1), 201–225 (1981).
23. J. Q. Feng, "A general fluid dynamic analysis of drop ejection in drop-on-demand ink jet devices," *J. Imaging Sci. Technol.* **46**(5), 398–408 (2002).
24. N. Link and R. Semiat, "Ink drop motion in wide-format printers I. Drop flow from drop-on-demand (DOD) printing heads," *Chem. Eng. Process.* **48**(1), 68–83 (2009).
25. T. M. Liou, K. C. Shih, S. W. Chau, and S. C. Chen, "Three-dimensional simulations of the droplet formation during the inkjet printing process," *Int. Commun. Heat Mass Transfer* **29**(8), 1109–1118 (2002).
26. K. S. Moon, J. H. Choi, D. J. Choi, S. H. Kim, M. H. Ha, H. J. Nam, and M. S. Kim, "A new method for analyzing the refill process and fabrication of a piezoelectric inkjet printing head for LCD color filter manufacturing," *J. Micromech. Microeng.* **18**(12), 125011 (2008).
27. F. X. Pan, J. Kubby, and J. K. Chen, "Numerical simulation of fluid-structure interaction in a MEMS diaphragm drop ejector," *J. Micromech. Microeng.* **12**(1), 70–76 (2002).
28. H. C. Wu, W. S. Hwang, and H. J. Lin, "Development of a three-dimensional simulation system for micro-inkjet and its experimental verification," *Mater. Sci. Eng., A* **373**(1–2), 268–278 (2004).
29. A. S. Yang, J. C. Yang, and M. C. Hong, "Droplet ejection study of a Picojet printhead," *J. Micromech. Microeng.* **16**(1), 180–188 (2006).
30. Y. Suh and G. Son, "A level-set method for simulation of a thermal inkjet process," *Numer. Heat Transfer, Part B* **54**(2), 138–156 (2008).
31. J. D. Yu, S. Sakai, and J. Sethian, "A coupled quadrilateral grid level set projection method applied to ink jet simulation," *J. Comput. Phys.* **206**(1), 227–251 (2005).
32. C. S. Kim, S. J. Park, W. Sim, Y. J. Kim, and Y. Yoo, "Modeling and characterization of an industrial inkjet head for micro-patterning on printed circuit boards," *Comput. Fluids* **38**(3), 602–612 (2009).
33. H. P. Le, H. P. Le, and T. P. Le, "Microfluid device and ultrasonic bonding process," U.S. Patent No. 6464324 B1 (Oct. 15, 2002).
34. R. Li, N. Ashgriz, and S. Chandra, "Droplet generation from pulsed micro-jets," *Exp. Therm. Fluid Sci.* **32**(8), 1679–1686 (2008).
35. H. Y. Gan, X. C. Shan, T. Eriksson, B. K. Lok, and Y. C. Lam, "Reduction of droplet volume by controlling actuating waveforms in inkjet printing for micro-pattern formation," *J. Micromech. Microeng.* **19**(5), 055010 (2009).
36. Q. Xu and O. A. Basaran, "Computational analysis of drop-on-demand drop formation," *Phys. Fluids* **19**(10), 102111 (2007).
37. W. J. Rider and D. B. Kothe, "Reconstructing volume tracking," *J. Comput. Phys.* **141**(2), 112–152 (1998).
38. D. B. Kothe, W. J. Rider, S. J. Mosso, J. S. Brock, and J. I. Hochstein, "Volume tracking of interfaces having surface tension in two and three dimensions," in *Proc. AIAA 34th Aerospace Sciences Meeting and Exhibit*, AIAA 96-0859, pp. 1–24, Reno, NV (1996).
39. J. U. Brackbill, D. B. Kothe, and C. Zemach, "A continuum method for modeling surface-tension," *J. Comput. Phys.* **100**(2), 335–354 (1992).
40. M. Renardy, Y. Renardy, and J. Li, "Numerical simulation of moving contact line problems using a volume-of-fluid method," *J. Comput. Phys.* **171**(1), 243–263 (2001).
41. H. A. Stone, B. J. Bentley, and L. G. Leal, "An experimental study of transient effects in the breakup of viscous drops," *J. Fluid Mech.* **173**, 131–158 (1986).
42. D. Henderson, H. Segur, L. B. Smolka, and M. Wadati, "The motion of a falling liquid filament," *Phys. Fluids* **12**(3), 550–565 (2000).
43. P. K. Notz and O. A. Basaran, "Dynamics and breakup of a contracting liquid filament," *J. Fluid Mech.* **512**, 223–256 (2004).
44. R. Schulkes, "The contraction of liquid filaments," *J. Fluid Mech.* **309**, 277–300 (1996).

Jr-Ming Lai received his MS degree in mechanical engineering from the National Chiao Tung University, Taiwan, with research involving the investigation of the effect of the pH of an aqueous solution on the thermal denaturation of double-stranded DNA. He is currently pursuing his PhD degree in mechanical engineering at the National Chiao Tung University, Taiwan.

Jenn-Der Lin received his BS degree in mechanical engineering from the Tamkang College of Art and Science, Taiwan, in 1975 and his MS and PhD degrees in mechanical engineering from the University of Oklahoma in 1980 and 1985, respectively. From 1985 to January 2010, he was associated with National Chiao Tung University, Hsinchu, Taiwan, where he chaired the Mechanical Engineering Department, and was the Dean of Student Affairs and later the Dean of Academic Affairs. His research includes microfluidics, thermal sciences, light scattering and its application, and biothermodynamics. He is currently president of the National Formosa University, Taiwan.

Kung Linliu received his BS degree in chemistry from National Taiwan Universty in 1986 and his PhD degree in polymer chemistry from State University of New York at Stony Brook in 1994. From 1995 to 2001, he was a technical manager of the Research and Development Division for the semiconductor process of the Taiwan Semiconductor Manufacturing Co. (TSMC), the Worldwide Semiconductor Manufacturing Corp. (WSMC), Macronix International Co. (MXIC), and Vanguard Intl. Semiconductor Corp. (VIS). From 2001 to 2010, his interest shifted to microelectromechanical systems (MEMS) devices and processes. He was a founder and CEO of an inkjet technology company, Printech International Inc. in 2002. He is currently an associated scientist with the National Synchrotron Radiation Research Center (NSRRC). His current research includes novel techniques for nanofabrication, new devices for nanoelectronics, and nanofluids applications.